

Comprehensive analysis of southern eclipsing systems with pulsating components: The cases of HM Pup, V632 Sco and TT Vel

A. Liakos¹, D. J. W. Moriarty², M. G. Blackford³, J. F. West⁴, P. Evans⁵, C. M. Moriarty⁴, and S. M. Sweet^{2,6}

¹ Institute for Astronomy, Astrophysics, Space Applications and Remote Sensing, National Observatory of Athens, Metaxa & Vas. Pavlou St., GR-15236, Penteli, Athens, Greece
e-mail: alliakos@noa.gr

² School of Mathematics and Physics, The University of Queensland, Queensland, 4072, Australia

³ Variable Stars South (VSS), Congarinni Observatory, Congarinni, NSW, 2447, Australia

⁴ Astronomical Association of Queensland, St. Lucia, Queensland, 4067, Australia

⁵ El Sauce Observatory, Coquimbo Province, Chile

⁶ ARC Centre of Excellence for All Sky Astrophysics in 3 Dimensions (ASTRO 3D), Australia

Received September XX, 2021; accepted March XX, 2021

ABSTRACT

This work presents an extensive analysis of the properties of three southern semi-detached eclipsing binaries hosting a pulsating component, namely HM Pup, V632 Sco, and TT Vel. Systematic multi-filtered photometric observations were obtained using telescopes located in Australia and Chile mostly between 2018-2021. These observations were combined with data from the Transiting Exoplanet Survey Satellite (*TESS*) mission for a detailed analysis of pulsations. Spectral types and radial velocities were determined from spectra obtained with the Australian National University's 2.3 m telescope and Wide Field Spectrograph. The data are modelled and the absolute parameters of all components are derived. The light curve residuals are further analysed using Fourier transformation techniques for the determination of the pulsation frequencies. Using theoretical models, the most probable modes of the principal oscillations are also identified. Eclipse-timing variation analysis is also made for all systems and the most likely mechanisms modulating the orbital period are proposed. The physical properties of these systems are compared with other similar cases and the locations of their components are plotted in the M-R and HR diagrams. Finally, the pulsational properties of the oscillating components are compared with currently known systems of this type within the orbital-pulsation period and log g -pulsation period diagrams. These systems are identified as oEA stars by definition, with the primaries to be pulsating stars of δ Scuti type, while evidence of mass flow from the evolved secondary components is present in their Na I D spectra.

Key words. stars:binaries:eclipsing – stars:fundamental parameters – (Stars:) binaries (including multiple): close – Stars: oscillations (including pulsations) – Stars: variables: delta Scuti – Stars: individual: HM Pup, V632 Sco, TT Vel

1. Introduction

A goal of asteroseismology is to improve the physics of stellar structure and evolution models by requiring such models to fit observed oscillation frequencies and modes of δ Scuti stars (Antoci et al. 2014). The single pulsating stars of δ Scuti type exhibit radial and non-radial oscillation modes triggered mostly by the κ -mechanism (c.f. Aerts et al. 2010; Balona et al. 2015). Their pulsations are, in general, relatively fast (20 min-8 h), and typically show multiperiodic behaviour. The masses of these stars range between 1.5-2.5 M_{\odot} (Aerts et al. 2010), their temperatures between 6100-9800 K (A-F spectral classes), their luminosity classes between III-V. They are located inside the classical instability strip and share a border in the Colour-Magnitude diagram (i.e. red-edge of the classical instability strip) with the γ Doradus pulsating stars, which oscillate in lower frequencies up to 4 cycle d^{-1} (Handler 1999). In an analysis of 750 A-F type stars, observed by *Kepler* mission (Borucki et al. 2010; Koch et al. 2010), Uytterhoeven et al. (2011) discovered that 63% are of δ Scuti or γ Doradus type or present hybrid behaviour. The latter result regarding the hybrid nature of these stars is an open question to date.

The eclipsing binaries (EBs) are the ultimate astrophysical tools for determining the absolute parameters of stellar compo-

nents. Their light curves (LCs) provide information about the luminosity and radius ratio of their components, as well as the orbital period, eccentricity and inclination of the system. The radial velocities (RVs) of both components are required for calculating the mass ratio of the system. That is extremely critical for modelling eclipsing systems accurately, compared to models using only photometric data (i.e. degeneracy of solutions). Thus, combining photometry and spectroscopy of the EBs and using the Kepler's third law, we are able to calculate stellar physical parameters with high accuracy. However, although the aforementioned methods concern the current status of an EB, using past eclipse timings and by applying the 'Eclipse Timing Variation' (ETV) method (also called as 'O-C analysis'), it is feasible to identify short-, mid- or long-term orbital period changes (such as cyclic or secular). These changes can be attributed to standard orbital period (P_{orb}) modulation mechanisms, such as mass transfer/loss, additional components orbiting the EB or even magnetic braking. Semi-detached Algol-type EBs have cool secondary stars that have filled their inner critical Lagrangian surface and are transferring mass to the hotter star, which was originally the less massive component. Emission in the H_{α} spectra of these systems has provided evidence of the mass flow and presence of circumstellar gas (Richards & Albright 1999). In systems where

arXiv:2204.13629v1 [astro-ph.SR] 28 Apr 2022

the cool component is very faint, H_α emission would only be detected during primary eclipses if the secondary component was larger than the hotter star. However, the Na I D lines of late K stars are relatively much stronger than those of their hot companions, thus they can reveal the presence of circumstellar gas at quadrature orbital phases, especially if the systemic velocity is large (Moriarty et al. 2019).

The high accuracy (order of 10^{-4} mag) and the continuity in time of the photometric data of *Kepler* (Koch et al. 2010; Borucki et al. 2010), *K2* (Howell et al. 2014) and Transiting Exoplanet Survey Satellite (*TESS*; Ricker et al. 2009, 2015) missions provide the means for detailed studies of stellar oscillations, especially in the case they are combined with multi-band photometry and high-resolution spectroscopy. The time resolution of the data of these missions vary from 2 up to 30 min and they are quite useful for the determination of short-period frequencies, such as those met in δ Scuti stars. Given their accuracy, they also provide the opportunity to detect low-amplitude pulsations of the order of a few μmag (c.f. Murphy et al. 2013; Bowman & Kurtz 2018; Liakos 2020b; Kurtz et al. 2020; Liakos & Niarchos 2020; Kim et al. 2021). Moreover, these missions provide long time-coverage (some times of the order of years) that is very useful for the calculation of many minima timings of EBs, which in turn, allows for a better study of their orbital period changes.

Eclipsing binary systems in which one component is a pulsating star are especially important in modern astrophysics as they provide the means to calculate the absolute properties of the pulsating star. The latter is quite significant and allows for the checking of stellar evolution theory and for the asteroseismology as well. Moreover, EBs hosting oscillating components and exhibiting mass transfer are very important in the field of asteroseismology, as they show different pulsational behaviour in terms of initiation, preservation and evolution in comparison with those that are members of detached systems or are single stars (Liakos & Niarchos 2017; Liakos 2017; Mkrтчichian et al. 2018b; Bowman et al. 2019). EBs of the Algol type, designated as oscillating eclipsing Algol (*oEA*) systems (Mkrтчichian et al. 2002), contain an active cool G-K giant or subgiant star that transfers mass to a hot (A-F type) mass-accreting primary star of the δ Scuti type.

Currently, more than 330 binary systems with a δ Scuti component are known (Liakos & Niarchos 2017; Liakos 2018, 2020a, and personal collection from literature from 2020 and later - available online¹). However, only 233 of these systems are EBs, while only 48 of these 233 are also double-line spectroscopic binaries (SB2), i.e. they can provide accurate absolute stellar properties. From these 48 EB+SB2 systems, only 21 are *oEA* stars, while the rest are in detached configurations. The aforementioned numbers indicate the difficulty and the importance in determining the absolute properties of pulsating stars in EBs.

This work is a continuation of the detailed study on individual *oEA* stars with a δ Scuti component (see also Liakos et al. 2012; Liakos & Niarchos 2013; Soyduđan et al. 2013; Liakos & Cagař 2014; Liakos 2017, 2018; Ulař et al. 2020) and the first paper of a series dedicated to southern systems. We report analyses of three EBs that were apparently single-lined: HM Puppis, V632 Scorpii and TT Velorum. These systems are previously known EBs exhibiting pulsations (Moriarty et al. 2013; Streamer et al. 2016; Mkrтчichian et al. 2018a, respectively) but there is no detailed study for any of them nor any classification for their

Roche geometry based on models to date. Therefore, this work enriches significantly the sample of *oEAs* with well determined absolute stellar properties by $\sim 14\%$ and the total number of known *oEAs* by $\sim 2.4\%$. For the selected systems, multi-band ground-based and space-borne photometric and low- and high-resolution spectroscopic data (see Section 2) have been collected in order to: a) perform a detailed modelling (Section 3), b) calculate the stellar parameters with high accuracy (Section 3), c) perform ETV analysis for the determination of the most possible orbital period modulating mechanisms (Section 4), d) detect the most powerful pulsation frequencies (Section 5), and e) estimate the oscillation modes (Section 5). The properties of the systems as well as the pulsation properties of their oscillating stars are compared with others of similar type (Section 6). Finally, summary and conclusions are given in Section 7. In all tables of the present study the errors of the parameters are given in parentheses alongside values and correspond to the last digit(s).

2. Observations, data reduction and analysis

In this study, three different data sources are used: a) Ground-based multi-band photometric time series, b) *TESS* data obtained with long- (30 min), mid- (10 min) and short-cadence (2 min) modes, and c) high and low resolution spectroscopic data for the RVs calculation and spectral type determination.

2.1. Ground-based photometry

The ground-based data were obtained from three different observatories located at the southern hemisphere. Small-size telescopes in Australia and Chile, equipped with CCD cameras and photometric filters, were employed for the observations. The majority of the data were collected between 2018-2021, however, for one system, data from 2013 and 2014 were also used in our study. The detailed observations log is given in Table 1, where we list: the name of the system, the observing site (inc. longitude and latitude), the telescope (diameter, focal ratio, and optical design), the camera (model, chip model, pixel size, and pixels array), the filter used (*Fil.*), the exposure time (*Exp.*) for the images in each band, the number of nights (*Nig.*) with data obtained for each filter, the date range of the observations (in DD/MM/YY format), and the total number of points for each filter. It should be noted, that in one night more than one filter might have been used. After the completion of the LC of the EB, the *B* filter observations continued around the quadratures of the systems for a longer time coverage of the pulsations.

The data reduction was made with various photometric packages, i.e. MaximDL (Diffraction Limited 2012); AstroImageJ (Collins et al. 2017), using the differential aperture photometry technique. The magnitude calibration of the variables was based on the respective apparent magnitudes of the comparison stars taken from the AAVSO Photometric All-Sky Survey (APASS) DR9 (Henden et al. 2015) and the differential magnitude (for details see Moriarty et al. 2019). The phase-folded LCs of the systems are given in Fig. 10.

2.2. TESS photometry

The *TESS* data were downloaded from the Mikulski Archive for Space Telescopes (MAST²) archive. The observations log for each system is given in Table 2, where the following are listed:

¹ <http://alexiosliakos.weebly.com/catalogue.html>

² <https://mast.stsci.edu>

Table 1. Ground-based photometric observations log.

System	Site	Telescope	Camera	Fil.	Exp. (s)	Nig.	Date range	Points
HM Pup	El Sauce, Chile 70.76°W, 30.47°S	35.6 cm, f/7.2 CDK ^a	SBIG STT 1603-3,	<i>B</i>	80-90	17	26/11/20-17/1/21	5225
			KAF-1603, 9 μ m,	<i>V</i>	60	15		5078
			1536×1024	<i>I</i>	90	11		2840
V632 Sco	Glen Aplin, Australia 151.85°E, 28.75°S	35.6 cm, f/11 S-C ^b	Moravian G3-6303	<i>B</i>	140	10	31/7/13,	772
			KAF-6303E, 9 μ m,	<i>V</i>	60	7	28/5/14,	670
			3072×2048	<i>I</i>	70	7	13-21/6/18	614
TT Vel	Congarinni, Australia 152.86°E, 30.73°S	35.5 cm, f/8 RC ^c	SBIG STT 3200-ME,	<i>B</i>	40-55	8	23/7-21/8/20	3106
			KAF-3200ME, 6.8 μ m,	<i>V</i>	40	2		926
			2184×1472	<i>I</i>	40	1		296
TT Vel	Congarinni, Australia 152.86°E, 30.73°S	35.5 cm, f/8 RC ^c	SBIG STT 3200-ME,	<i>B</i>	45	26	20/4-20/6/21	2621
			KAF-3200ME, 6.8 μ m,	<i>V</i>	30	19		507
			2184×1472	<i>I</i>	45	19		491

Notes. ^aCorrected Dall-Kirkham, ^bSchmidt-Cassegrain, ^cRitchey-Chrétien

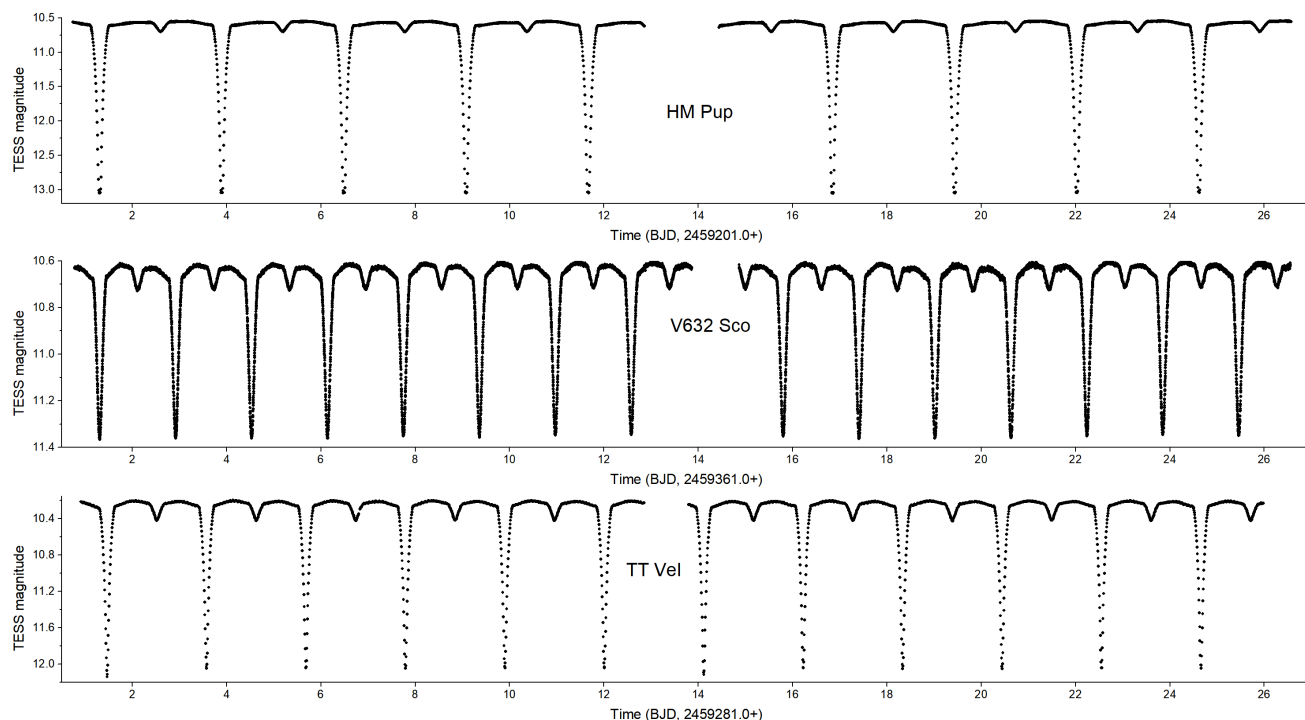


Fig. 1. *TESS* LCs that cover approximately 26 days of continuous monitoring. The rest data are not shown for scaling reasons. The time resolution of the data sets is 10, 2, and 10 min for HM Pup (top), V632 Sco (middle), and TT Vel (bottom), respectively.

Table 2. *TESS* observations log.

System	m_{TESS} (mag)	BJD begin	Days	Sr	Res. (min)	Points
HM Pup	10.55	2458491.85	24.16	7	30	1000
		2458518.10	23.83	8	30	682
		2459201.73	25.83	33	10	3495
		2459228.76	25.31	34	10	3645
		2459255.00	24.98	35	10	3597
V632 Sco	10.62	2458624.97	27.90	12	30	1244
		2459361.78	27.84	39	2	18330
TT Vel	10.21	2458544.56	23.85	9	30	940
		2458571.72	23.92	10	30	878
		2459280.91	25.08	36	10	3612

the BJD of the beginning, the number of continuous days of observations, the sector (Sr) of *TESS*, the time resolution ($Res.$), and the number of points of each data set.

For all systems, the Pre-search Data Conditioning Simple Aperture Photometry (PDCSAP) flux, which typically is corrected for long-term trends caused by instrumental effects, was used, when available. However, in the data sets where the PDC pipeline produced distorted LCs, the SAP flux values were used instead. The magnitudes of the systems (assumed as the maximum brightness values) were taken from the *TESS* Input Catalog v8.0 (Stassun et al. 2019) and were used for the flux-to-magnitude conversion (Table 2).

For HM Pup, there are five data sets, two in long- and three in mid-cadence modes. For the latter ones (i.e. data sets of sectors 33-35), although PDCSAP flux values are available, they present obvious distortions, therefore the SAP fluxes were used. V632 Sco was observed in long- and short-cadence modes. For the long-cadence data set, only the SAP flux is given, while the PDCSAP flux values are available for the short-cadence set. The time-series data sets for TT Vel were made in long- and mid-

Table 3. Spectroscopic observations log. All data were obtained with the WiFeS instrument on the 2.3 m ANU telescope.

System	Date range	Phase	Spectra	Expos. (s)	Grating	
HM Pup	30/4/18	0.00	2	1100	B3000 (S/N=150)	R7000 (S/N=140)
	28/5/21	0.00	2	1000	B3000 (S/N=150)	R7000 (S/N=140)
	28/3/21	0.50	3	100	B3000 (S/N=210)	
V632 Sco	14/2/17-27/5/21	0.20-0.36; 0.62-0.88	41	180-420	B7000 (190<S/N<250)	R7000 (200<S/N<250)
	12/6/17	0.50	3	60	B3000 (S/N=220)	
TT Vel	2/5/18-8/7/20	0.17-0.32; 0.65-0.75	23	100-420	B7000 (340<S/N<370)	R7000 (270<S/N<360)
	26/4/21	0.50	3	60	B3000 (S/N=130)	
	1/12/20 - 28/5/21	0.16-0.32; 0.66-0.85	35	180-420	B7000 (350<S/N<160)	R7000 (340<S/N<500)

cadence modes. The PDCSAP flux was available, but as in the case of HM Pup, there are lots of distortions, thus, the SAP flux values were again used. Samples of the *TESS* LCs for all systems are plotted in Fig. 1, while the folded data in the orbital period are given in Fig. 10.

2.3. Spectroscopy

Spectra were observed with the wide field spectrograph (WiFeS) mounted at the Nasmyth focal position of the Australian National University's 2.3 m telescope at Siding Spring Observatory, Australia (Dopita et al. 2007, 2010). The spectrograph is equipped with two Fairchild Imaging CCDs with a resolution of 4096×4096 pixels and a pixel scale of 0.5 arcsec. The 560 nm dichroic beam splitter was used. The detailed spectroscopic observations log is given in Table 3 and includes for each system: the date range (in DD/MM/YY format), the orbital phase of the system at the time of observations, the number of the obtained spectra and the corresponding exposure time (*Expos.*), and the grating used along with the resulting signal-to-noise (S/N) ratio. See Moriarty et al. (2019) for details of the procedures used to determine RVs and spectral types. In general, for RV determinations, sets of three or four spectra were observed at each phase with the B7000 grating, together with a spectrum of the Ne-Ar arc lamp before and after each set or closely grouped sets. Exposure times with the B7000 grating were long enough to allow detection of the faint secondary stars' metal lines with the broadening function in RAVESPAN (Pilecki et al. 2017). On several occasions, at the same time as long exposure times were used with the B7000 grating, shorter exposure times were used with the R7000 grating to enhance the separation of Na I D lines of the primary stars from the lines due to circumbinary gas. As HM Pup is a totally eclipsing system, spectra of its secondary component can be observed during the 42 minute period of totality. We observed it twice with the B3000 grating for spectral classification and with the R7000 grating to seek evidence of chromospheric activity and mass flow.

2.3.1. Spectral classification

Spectra for classification were observed with the low-resolution B3000 grating (708 lines mm⁻¹, R=3000). Its wavelength range of 3200 to 5900 Å includes the Balmer lines from H_β-H_γ, and the important Ca I K line (the Ca II H line is blended with H_ε in the spectra of the A and F-type stars in the systems studied here). The spectra of the primary components of HM Pup, V632 Sco, and TT Vel were observed during the secondary eclipse (phase 0.5) with short exposures to exclude interference by their faint secondary components. The secondary component of HM Pup was observed at phase 0.0. All these spectra were corrected to

heliocentric values by subtracting the systemic radial velocities of 58, -17, and 24 km s⁻¹ respectively (see Table 4). Spectral types were determined using 'XCLASS' and 'MKCLASS' programmes (Gray & Corbally 2014). XCLASS provides direct comparison of the target spectrum with reference spectra from the MKCLASS³ libraries, which encompass integer spectral temperature types from O6 to M5, and a wide range of luminosity types between V and Ia. The target spectra were normalised to unity at 4503 Å to match the library spectra.

We classified the spectra initially by visual comparisons with selected reference spectra across the wavelength range of 3800-4600 Å. The best fits of the primary stars were HM Pup: A6V, V632 Sco: F2V and TT Vel: A8V. We classified the HM Pup secondary star as K8IV/III. The spectra were rectified to deliver a linear continuum baseline using the 'Autorectify' function in the XMK25 display routine in XCLASS (Fig. 2). These were then compared with other reference spectra, including the examples provided in the work of Gray & Corbally (2009).

2.3.2. Radial Velocities

In general for radial velocity determinations, sets of three or four spectra were observed at each phase with the high-resolution B7000 grating (1530 lines mm⁻¹, R=7000) that provides a velocity resolution of 45 km s⁻¹ and wavelength range between 4180-5580 Å. Exposure times were long enough to allow detection of the metal lines of the faint secondary stars with the broadening function method in RAVESPAN software (Ruciński 1992, 2002; Pilecki et al. 2017). Spectra in the phase ranges shown in Table 3 were analysed. The optimum settings used for the three systems studied here were as follows. Spectra were normalised and analysed in the wavelength range 4355-4840 Å and 4880-5548 Å with the Balmer line masked. A template with an effective temperature of 4000 K, gravity coefficient set at 2.5 and metallicity at 0.0, was selected from the synthetic spectra supplied with the RAVESPAN software (Coelho et al. 2005). A 4th-order polynomial was used with resolution set at 2.0 km s⁻¹ and v-range 1.8. With these settings, the broadening function velocity peak of the secondary components was clearly evident (Fig. 3). The phased RVs curves are plotted in Fig. 10, while the complete list of RV values is given in Table A.1 in App. A.

2.3.3. Chromospheric activity and gas streaming

Emission was observed in the centres of the Ca II H and K lines of the secondary component of HM Pup during the total primary eclipse. The emission peaks had a red shift of 58 km s⁻¹ from the systemic velocity, indicating they were due to chromo-

³ <http://www.appstate.edu/~grayro/mkclass/>

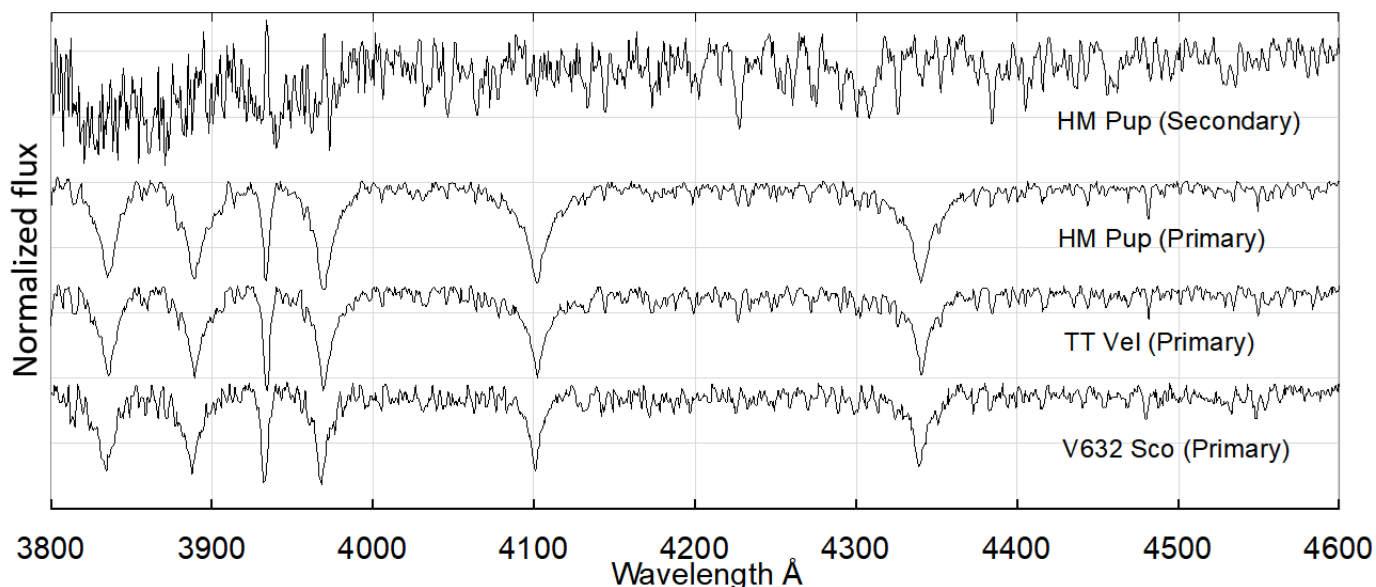


Fig. 2. Rectified spectra of the primary components of each system and the secondary component of HM Pup.

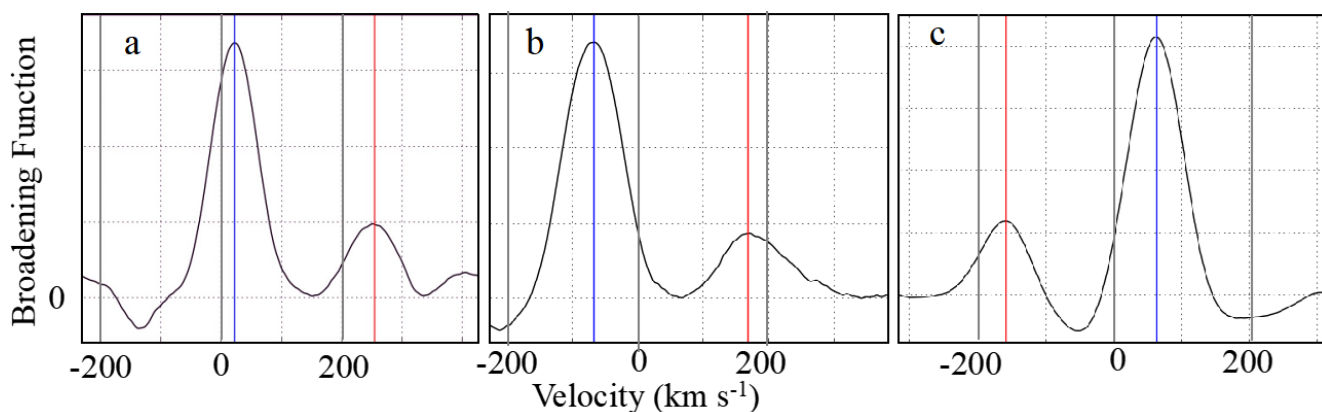


Fig. 3. Examples of Broadening Functions method on the spectra of (a) HM Pup at phase 0.25, (b) V632 Sco at phase 0.25, and (c) TT Vel at phase 0.75. Blue lines denote the RVs of the primary and red lines those of the secondary components.

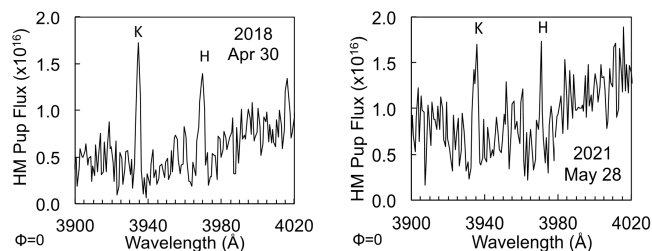


Fig. 4. Spectra of the HM Pup secondary star in the range 3900-4020 Å (with $R=3000$) during totality on two occasions. The K and H emission peaks have a red shift of 58 km s^{-1} .

spherical activity and not circumbinary gas (Fig. 4). On the same nights, the H_{α} spectra had an emission peak with a blue shift of 120 km s^{-1} and the absorption line was broadened with a red shift from 33 to 110 km s^{-1} (Fig. 5). The Na I D lines of the secondary component on those nights were broadened towards red at velocities of $110\text{-}170 \text{ km s}^{-1}$ (Fig. 5). Sky background flux values were subtracted from all the spectra in Figs 4 and 5, as the exposures used were long. The sky background flux values in all spectra in Figs 6 and 7 were 2-3 orders of magnitude lower than the stellar flux values; the difference was similar to that found

for ST Cen and V775 Cen (Moriarty et al. 2019). Flux units are $\text{ergs cm}^{-2} \text{ s}^{-1} \text{ arcsec}^{-2} \text{ \AA}^{-1}$.

Broadening or splitting in the spectra of the sodium D doublet lines at different phases indicates evidence of gas streaming from the secondary components of Algol systems (see Moriarty et al. 2019). Circumstellar gas was particularly evident around HM Pup. The primary component's sodium D line centres at phase 0.75 are red-shifted with a velocity of 103 km s^{-1} (the sum of the orbital and systemic velocities of 45 and 58 km s^{-1} respectively). A clear separation of the sodium lines of the slower moving gas from the photospheric Na I D absorption lines of the receding primary star itself is clearly evident. Conversely, at phase 0.25, the sodium D lines of the approaching primary component were blended with the gas lines, which are evident as a broadening of the lines to the red (compare Fig. 6a-d with Fig. 6e-h).

In contrast to HM Pup, the sodium D line centres of V632 Sco, which has a negative systemic velocity, are blue shifted at phase 0.25 with a velocity of -69 km s^{-1} , (the sum of the orbital and systemic velocities of -52 and -17 km s^{-1} respectively). The narrow lines to the red side are evidence of circumstellar gas (Fig. 7a). At phase 0.75 the circumstellar gas lines are blended with those of the primary component, which are ro-

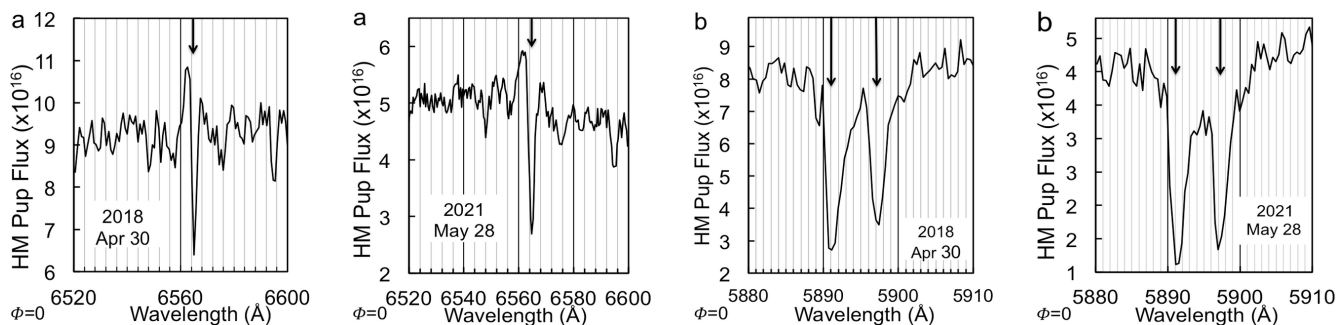


Fig. 5. The H_{α} (a) and Na I D (b) spectra of the HM Pup secondary star observed at the same time as the Ca II spectra in Fig. 4, but with $R=7000$. Arrows mark the calculated wavelength positions of the spectral line centres at the systemic velocity.

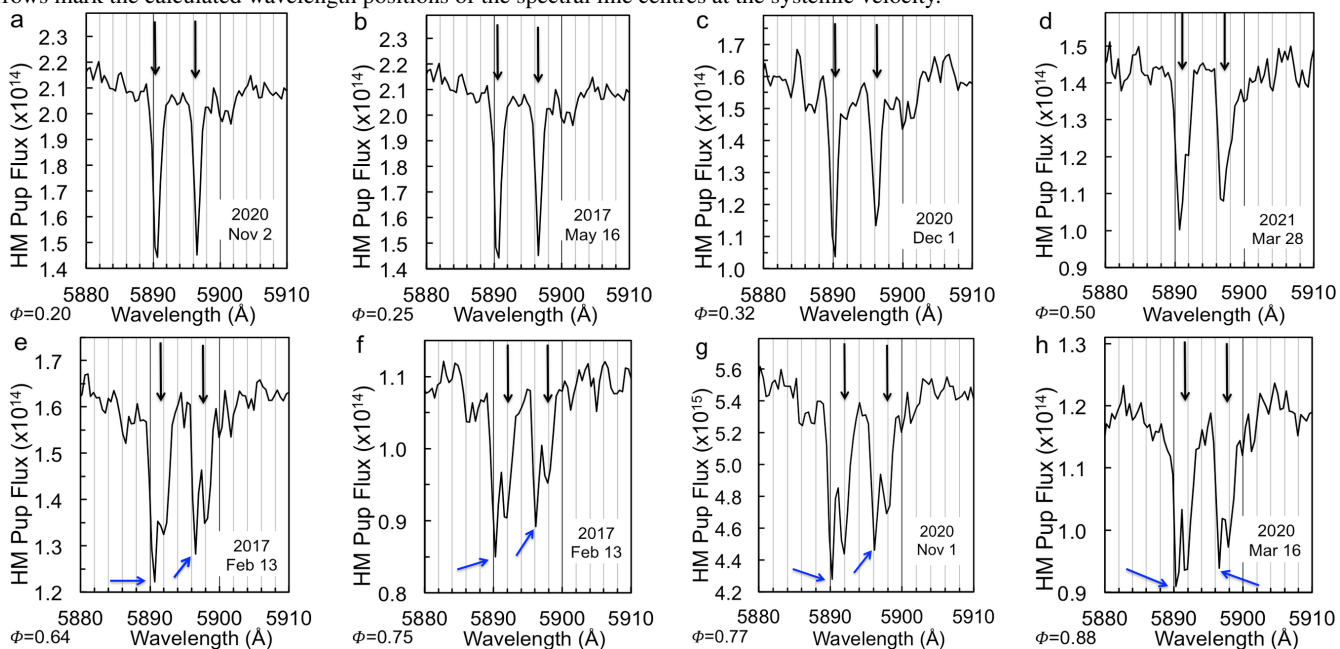


Fig. 6. Spectra of HM Pup Na I D lines at several orbital phases (Φ) with $R=7000$. Downward arrows mark the calculated position of the line centres for the primary star that are the sum of the systemic and orbital velocities. Lines of circumstellar gas are marked with blue arrows.

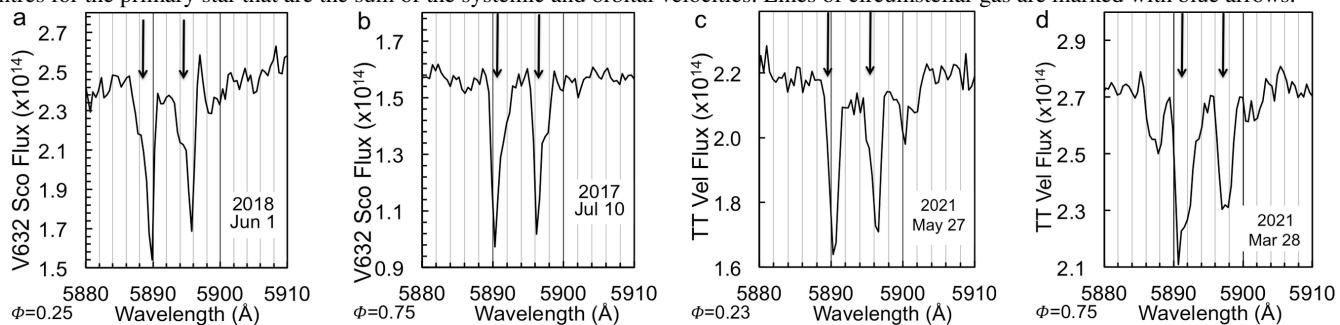


Fig. 7. Spectra of Na I D lines at quadrature phases ($R = 7000$): (a, b) V632 Sco, (c, d) TT Vel. Downward arrows mark the calculated position of the line centres for primary components that are the sum of their orbital and systemic velocities.

tationally broadened (Fig. 7b). There was also evidence of circumbinary gas in the Na I D spectra of TT Vel, but its stellar and gas sodium lines were similarly blended at the resolution available to us (Fig. 7c, d). The sodium lines of the primary components of each system were strong in comparison to those of their secondary stars, which have low luminosities.

The Na I D absorption lines of circumbinary gas, seen against the continuum of the primary star of HM Pup, are distinctly separate from the Na I D lines of the stellar photosphere at phases between 0.6 and 0.9, as shown in Fig. 6. The Full Width at Half Maximum (FWHM) of the primary component's absorp-

tion lines is 1.5 \AA , based on the primary star's rotational surface velocity; its velocity relative to the observer determines its central wavelength. Using these values, we were able to estimate the central position of the gas stream Na I D absorption lines at phases between 0.24 and 0.5 within the blended lines. This is illustrated in Fig. 8 for phase 0.28; the centre of the stellar Na I D2 line was determined to be 5890.24 \AA . The shape of the blended absorption line indicates the line centre of the gas stream is 5890.68 \AA .

This method was used to estimate the observed velocities of the gas along the observer's line of sight, and thence its veloc-

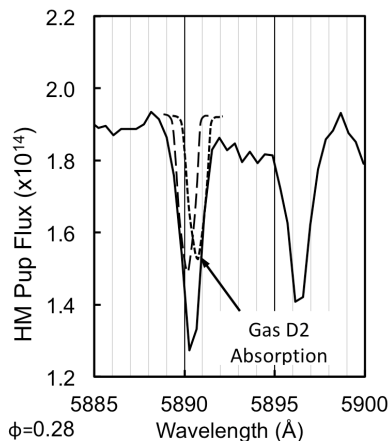


Fig. 8. Illustration of the method used to estimate the wavelength of the D2 line of the gas at phase 0.28. The primary star absorption line is long-dashed, the gas is short-dashed.

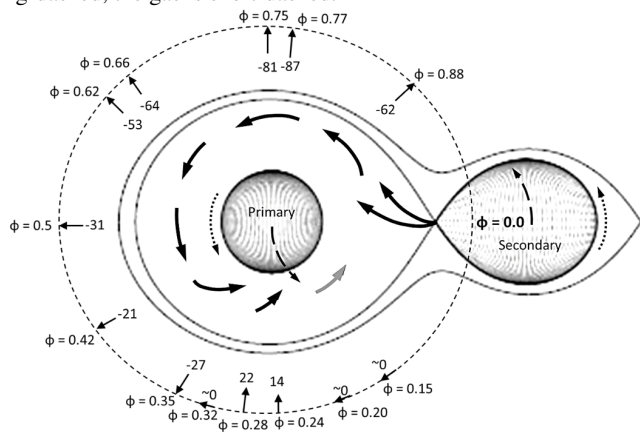


Fig. 9. Estimated path of the HM Pup gas stream. The phases of the observations are marked around the periphery of the dashed circle, the corresponding observed gas velocity and direction relative to the primary star are indicated inside the circle. The orbital direction and direction of rotation of the two stars are shown by the long-dashed and short-dashed arrows respectively. The wavelengths and velocities were adjusted, for clarity, to remove the fixed systemic velocity of 58 km s^{-1} .

ity relative the primary star at a range of phases. These velocities (listed in Table B.1) were used to determine an approximate path for the gas streaming from the secondary star and around the primary (Fig. 9). The gas is shown as leaving the secondary star at the first Lagrangian point and orbiting the primary star (at least in part). The velocity and direction of the gas flow within this region are reflected in the observed gas velocities, particularly those between phases 0.24 and 0.32, where the gas appears to fall on to the primary star. A transient accretion cloud or annulus could be present, depending on the rate of mass loss from the secondary star. As discussed by Richards & Albright (1999), accretion disks do not develop around EBs with short orbital periods.

3. Light and radial velocities curves modelling and absolute parameters calculation

The light and radial velocity curves of the three systems were analysed with ‘PHOEBE’ v.0.29d software (Prša & Zwitter 2005), which uses the 2003 version of the Wilson–Devinney code (Wilson & Devinney 1971; Wilson 1979, 1990). Temperatures, T , of the components were given values derived from

the spectral classification (see Section 2.3.1) and the spectral type-temperature correlation of Cox (2000). The temperatures of the primary components were kept fixed during the analysis, while those of the secondaries were adjusted. For all systems, the albedos, A and gravity darkening coefficients, g , of the components were given values according to their spectral types (Ruciński 1969; von Zeipel 1924; Lucy 1967). As the maxima of the LCs are displaced towards the secondary minimum (typically between phases 0.25-0.45 and 0.55-0.75) as a result of reflection due to the heating of the secondary components’ atmospheres by the hot primary components, A_2 was adjusted. The (linear) limb darkening coefficients, x , for the B , V , and I filters were taken from the tables of van Hamme (1993), while those for the $TESS$ photometric system, x_{TESS} , from Claret (2018, Table 5 in that work). The dimensionless potentials Ω and the fractional luminosity of the primary component L_1 , were also adjusted during the modelling. The systemic radial velocity, V_{sys} , the mass ratio, q , and the inclination of the system, i , were set as free parameters. As the three systems exhibit cyclic orbital period modulations (see Section 4) that could potentially be attributed to tertiary component(s), the third light parameter, l_3 , was tested initially, but it converged to a zero value in each case, and was, therefore, excluded from further modelling.

Intense magnetic dynamo activity is expected in close EBs with convective outer regions and rapid rotation rates locked to their orbital velocities (see Berdyugina 2005). The magnetic activity causes variability or asymmetry in LCs which could affect the modelling results. Several LC cycles for each system were obtained from the $TESS$ data (see Table 2). We carefully examined them to determine the stability of the asymmetries in successive LCs, and then decide how to proceed with the model. There were 20 and 12 complete LCs of mid-cadence data for HM Pup and for TT Vel, respectively, which, although displaying some variability, were sufficiently stable for modelling over the time range of the observations. However, in the case of V632 Sco there were 12 complete LCs of short-cadence data which show noticeable changes every few days. Therefore, for this system we modelled three groups of four LCs folded into the P_{orb} .

Given that the purpose of this work concerns mostly the asteroseismology of these systems, we excluded the long-cadence data of the systems from the modelling and kept only those with the best available time resolution. However, the long-cadence data were used for minima timing calculations (see Section 4). As with the $TESS$ data, the ground-based observations obtained in different time periods show asymmetries that cannot easily be fitted in a unique phased LC. In order to avoid this in our study, we again modelled the LCs of each system separately according to the asymmetries found. In particular, as V632 Sco is more active than the other two systems, in order to have complete LCs for the modelling, photometric observations in the V and I pass-bands over several years were combined. The examination of the LCs was made with great care, as the LC residuals are used later for frequency analysis. They must, therefore, be kept free of any proximity or stellar magnetic activity effects.

During the modelling process, all LCs from each pass-band were used initially with the RVs to derive the mean model of each system. Then, the values from the output of the mean model were used as initial inputs to model the individual phase-folded LCs (or groups of LCs) mostly by adjusting the spot parameters, namely Co-latitude, longitude, radius, and temperature factor. Thus, the parameters of the final model of each system are the average of the respective parameters of each LC model, and their uncertainties are the standard deviations. This procedure gives

Table 4. Modeling and physical parameters results.

	HM Pup		V632 Sco		TT Vel	
	System parameters					
T_0 (HJD)	2456306.998(1)		2458285.110(1)		2459329.957(13)	
P (d)	2.5897239(2)		1.610163(1)		2.10846(2)	
i ($^\circ$)	89.7(3)		78.4(1)		88.8(6)	
q (K_1/K_2)	0.243(9)		0.255(14)		0.232(8)	
V_{sys} (km s^{-1})	58(1)		-17(1)		24(1)	
	Components parameters					
	<i>Primary</i>	<i>Secondary</i>	<i>Primary</i>	<i>Secondary</i>	<i>Primary</i>	<i>Secondary</i>
T_{eff} (K)	8000(150) ^a	3915(35)	7000(150) ^a	3734(186)	7600(150) ^a	4515(66)
Ω	5.21(5)	2.370(1)	3.79(7)	2.369(1)	4.69(2)	2.332(9)
K (km s^{-1})	45(1)	185(2)	52(3)	205(4)	39(1)	167(2)
A	1 ^b	1 ^b	1 ^b	0.92(1)	1 ^b	0.86(1)
g^b	1	0.32	1	0.32	1	0.32
r_{pole}	0.202(1)	0.250(1)	0.282(1)	0.250(1)	0.225(1)	0.244(1)
r_{point}	0.204(1)	0.365(1)	0.290(1)	0.364(3)	0.227(1)	0.357(3)
r_{side}	0.203(1)	0.261(1)	0.287(1)	0.260(1)	0.226(1)	0.254(1)
r_{back}	0.204(1)	0.293(1)	0.289(1)	0.293(1)	0.227(1)	0.287(1)
x_B	0.592	0.999	0.605	1.001	0.612	0.948
x_V	0.516	0.866	0.497	0.812	0.533	0.797
x_I	0.352	0.628	0.338	0.592	0.365	0.571
x_{TESS}	0.229	0.565	0.298	0.468	0.237	0.496
$L/(L_1 + L_2)$ (B)	0.976(1)	0.024(1)	0.976(1)	0.024(1)	0.930(1)	0.070(1)
$L/(L_1 + L_2)$ (V)	0.947(1)	0.053(1)	0.973(1)	0.027(1)	0.884(1)	0.116(1)
$L/(L_1 + L_2)$ (I)	0.866(1)	0.134(1)	0.938(3)	0.062(1)	0.803(1)	0.197(1)
$L/(L_1 + L_2)$ (TESS)	0.877(1)	0.123(1)	0.919(1)	0.081(1)	0.816(1)	0.184(1)
	Physical parameters					
M (M_\odot)	2.65(9)	0.65(4)	2.4(1)	0.61(9)	1.55(6)	0.36(3)
R (R_\odot)	2.39(3)	2.99(3)	2.39(5)	2.11(5)	1.94(3)	2.12(3)
L (L_\odot)	21(1)	2.4(3)	12.2(9)	0.78(9)	11.2(9)	1.7(2)
$\log g$ (cm s^{-2})	4.11(2)	3.30(3)	4.06(3)	3.57(6)	4.05(2)	3.34(4)
a (R_\odot)	2.31(5)	9.5(1)	1.70(8)	6.7(1)	1.62(5)	7.0(1)
M_{bol}	1.4(4)	4.1(3)	2.0(4)	5.0(9)	2.1(5)	4.2(4)

Notes. ^ataken from spectroscopy (Section 2.3.1), ^bassumed

more realistic uncertainty values in comparison with the direct errors derived from ‘PHOEBE’ (c.f. Liakos 2017, 2018). Three modes of LC analyses were tried: mode 2 (detached system), mode 4 (semi-detached system with the primary component filling its Roche lobe) and mode 5 (conventional semi-detached binary); models for the three systems converged in mode 5. Therefore, all of them are semi-detached systems with their secondary components (less massive and cooler) filling their Roche lobes; thus, they are classical Algols (from evolutionary point of view). The amplitudes K_1 and K_2 were calculated using sinusoidal fittings on the respective RVs. The (linear) ephemeris of each system, i.e. the orbital period, P_{orb} , and a reference time of a primary minimum, T_0 , was based on the observed times of minima between 2012–2020 (see Section 4). The absolute parameters of the components were calculated based on the modelling results using the ‘AbsParEB’ software (Liakos 2015, mode 3). The upper and middle parts of Table 4 list the LCs and RVs modelling parameters, while its lower part the absolute parameters of the components. The fit on the LCs and RVs for all systems are given in Fig 10. The spots parameters for each system are given in Table C.1 in Appendix C.

4. Orbital period variation analyses

In order to determine whether orbital periods of the systems have changed, accurate eclipse times over a long term are necessary in order to apply an ETV analysis. For this, the first step was to gather the past times of minima from the literature and relevant minima databases and calculate new ones from our ground-based LCs as well as from the *TESS* data. Subsequently, these minima timings were used for the construction of the ETV plots and were fitted by various curves that correspond to different orbital period modulating physical mechanisms.

Times of minima of the systems observed at the Congarinni, El Sauce and Glen Aplin observatories were calculated in PERANSO⁴ from a 7th order polynomial fit to the light curves spanning two hours each side of the minima. Past times of minima were collected from the ‘O-C gateway’⁵, ‘TIDAK’⁶ (Ogloza et al. 2022, Timing DAtabase at Krakow; former O-C atlas; private communication with B. Zakrzewski) and the International Variable Star Index (VSX) databases⁷ and other literature sources containing times of minima. For eclipses observed in multiple filters in the same night, the average of the timings de-

⁴ <http://www.peranso.com/>

⁵ <http://var2.astro.cz/ocgate/>

⁶ <https://www.as.up.krakow.pl/tidak>

⁷ <https://www.aavso.org/vsx/>

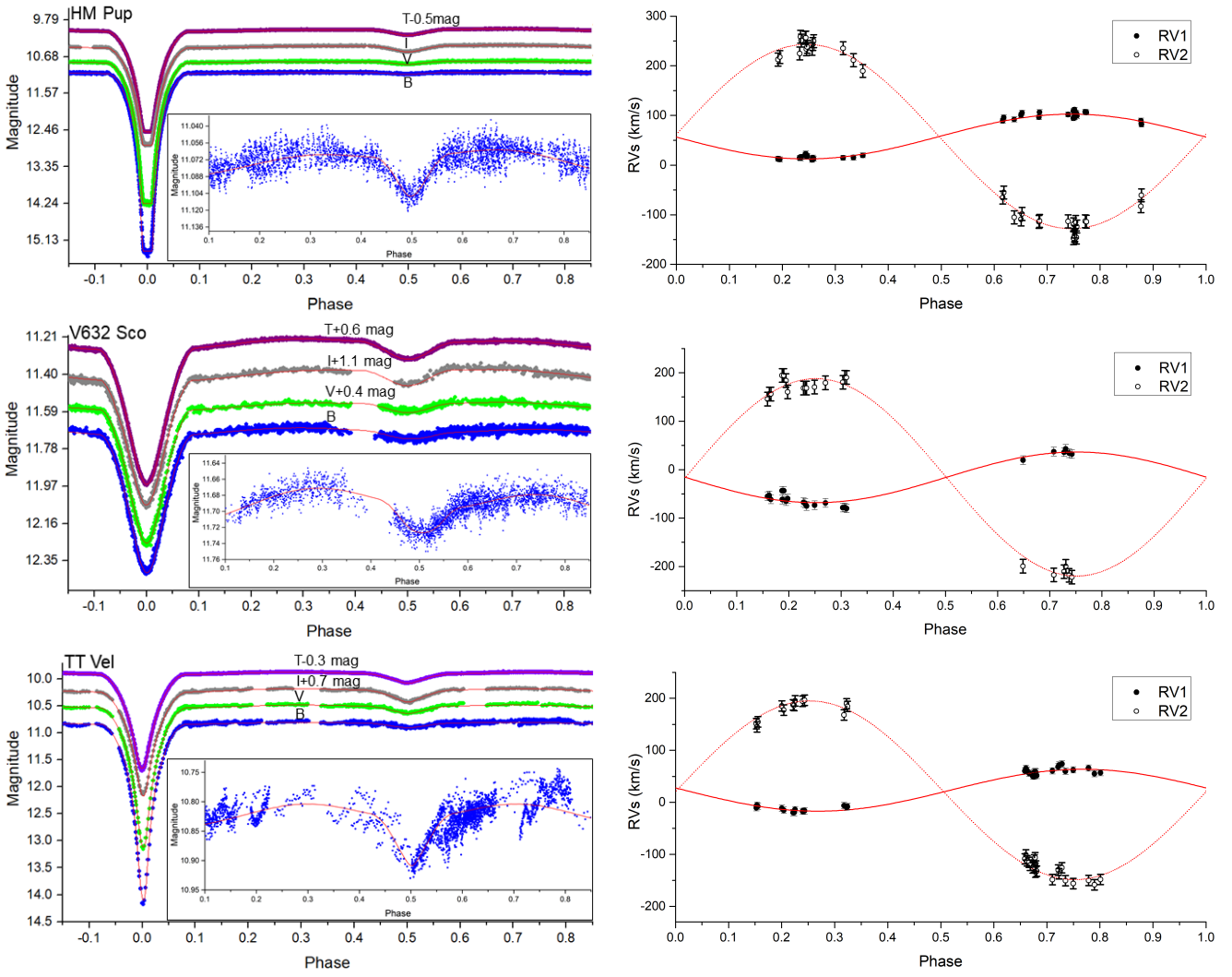


Fig. 10. Synthetic (solid lines) over observed (points) LCs (left plots) and RVs (right plots) for HM Pup (top panels), V632 Sco (middle panels), and TT Vel (bottom panels). Some LCs are vertically shifted for scaling reasons. The fit on the out-of-primary eclipse points of *B* filter is re-scaled and plotted allowing for better viewing.

rived from each filter was used. All available TESS data sets (see Table 2) were used for minima timing derivations. Due to the huge amount of observations in each data set, the software ‘B-Minima’ v.1.2 (Nelson 2005) was used; it searches and calculates minima timings automatically in big files. The calculated times of minima are given in Table D.1 in Appendix D.

The mass transfer/loss mechanisms that are expected to occur in semi-detached EBs were tested for the studied systems. Mass transfer stipulates secular changes of P_{orb} , while the ETV points present parabolic distribution, whose curvature indicates the direction of the mass transfer (i.e. upward means mass transfer from the less to the more massive component). The parabolic coefficient C_2 can be determined by fitting a parabola on the data points, and is used to calculate the P_{orb} change rate (\dot{P}) using the following equation (c.f. Kalimeris et al. 1994):

$$\dot{P} = \frac{2C_2}{P_{\text{orb}}}. \quad (1)$$

In the case of conservative mass transfer, the mass transfer rate (\dot{M}_{tr}) is calculated with the following equation (c.f. Kruszewski 1966; Hilditch 2001):

$$\dot{M}_{\text{tr}} = \frac{\dot{P} M_1 M_2}{3P_{\text{orb}} (M_1 - M_2)}, \quad (2)$$

where M_1, M_2 are the masses of the components of the EB.

Mass loss from EB systems can be due to stellar winds. This mechanism causes an increase in the orbital period, which is reflected as an upward parabolic distribution of the ETV points. The mass loss rate, \dot{M}_{loss} , is computed according to the formula of Hilditch (2001):

$$\dot{M}_{\text{loss}} = -\frac{M_1 + M_2}{2P_{\text{orb}}} \dot{P}. \quad (3)$$

Cyclic changes of the orbital period can be explained by either the Light-Time effect Irwin (1959, LITE) or with variations in magnetic cycles that could also modulate changes in eclipse timing due to the effect of star spots or with changes in the magnetic quadrupole moment in the secondary star (Applegate mechanism Applegate & Patterson 1987; Applegate 1992; Lanza et al. 1998; Hoffman et al. 2006; Rovithis-Livaniou et al. 2000; Lanza & Rodonò 2002). Applegate’s mechanism, however, is not likely to contribute significantly to period modulation in systems like those in this study (Lanza 2006; Völschow et al. 2018). An alternative mechanism involving a persistent non-axisymmetric internal magnetic field in the active component (Lanza 2020) may explain the observed ETV. However, an in deep examina-

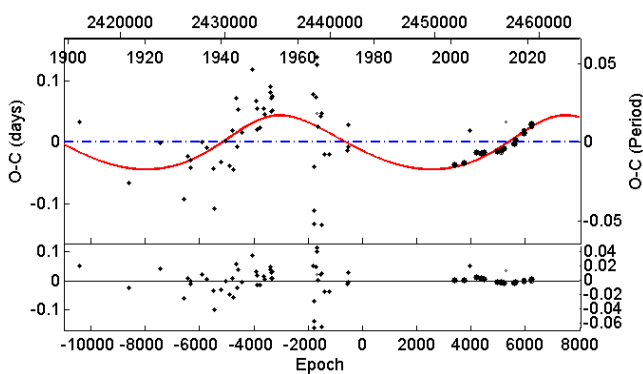


Fig. 11. Eclipse timing variations plot for HM Pup. Top panel: The $O-C$ points of the system fitted by a LITE curve (upper part) and the residuals (lower part) of the fit. For both panels, the bigger the symbol the bigger the statistical weight of the individual points.

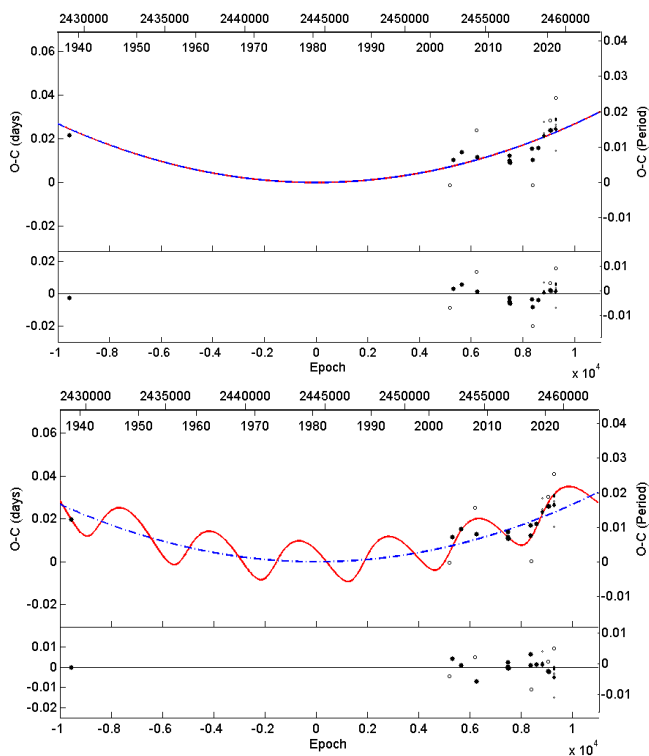


Fig. 12. Eclipse timing variations plots for V632 Sco. Top panel: The $O-C$ points of the system fitted by a parabola (upper part) and the residuals (lower part) of the fit. Bottom panel: The same as previous, but with the fit of a parabolic and a LITE curves.

tion of the cyclic modulations of the orbital periods of the systems are beyond the scope of this study.

Eclipse times were analysed with the *LITE* code of Zsche et al. (2009) that uses the method of statistical weights according to method used for the observations of the eclipses. Statistical weights, w , were applied as follows: for visually or photographically determined minima were assigned $w = 1$, and the photoelectric and CCD minima $w = 10$. This method works well when the minima timings are spread uniformly in time. For V632 Sco and TT Vel, most eclipse times were obtained after the year 2000. Moreover, there are a lot of minima timings from the *TESS* mission that cover only one or two years. In order to avoid over-weighting only one part of the ETV distribution, the *TESS* data were given $w = 1$ instead of 10. Using this

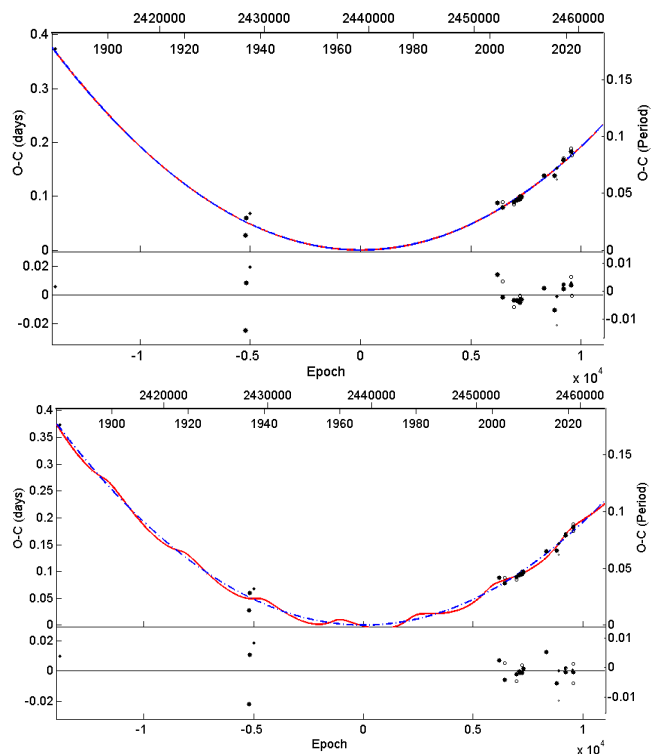


Fig. 13. The same as Fig. 12, but for TT Vel.

method, the many data points gathered within a short time range do not drag the fitting functions on them. In addition, minima timings based on the data of ASAS (Pojmanski 2002), ASAS-SN (Shappee et al. 2014) and Catalina (Drake et al. 2009) surveys (included in the TIDAK database) were given $w = 1$ due to their large uncertainties.

The code can fit one parabola and up to two LITE curves simultaneously. The initial ephemerides used for the ETV diagrams of the systems were taken from the ‘TIDAC’ and ‘O-C gateway’ databases. The ephemeris (T_0 -reference time of minimum and P_{orb}), the period of the modulation P_3 , the amplitude of the ETV variation A_{ETV} , the argument of periastron ω_3 , the eccentricity e_3 , and the time of the periastron passage T_{per} of the additional body are the free parameters of each LITE fitting curve. Moreover, the parabolic coefficient C_2 is also adjusted when parabola is selected for fit (for more details see Zsche et al. 2009). The selection of the final model is based on the Bayes Information Criterion (BIC).

Analyses of eclipse times of HM Pup did not show evidence of mass transfer, i.e. no secular changes were detected, but one possible cyclic variation (Fig. 11). The results from a LITE curve fit are shown in Table 5. The proposed mass of the additional component would require a comparable large luminosity, but there was no evidence for that in our spectroscopic observations nor in the LCs analysis. Therefore, other modulating mechanisms need to be tested for the explanation of this cyclic change. Moreover, a second LITE curve was tested because the data points after 2000 show evidence of an additional cyclic change. However, this LITE curve was proven statistically insignificant based on the BIC and was excluded.

For V632 Sco there was only one published time of minimum before the year 2000, i.e. in 1939. A parabola was chosen to fit the data (Fig. 12-top panel), but the residuals show an additional cyclic distribution. Therefore, a LITE curve was also tested and is plotted in Fig. 12 (bottom panel). Results for

Table 5. ETV analysis results.

System	HM Pup	V632 Sco	TT Vel
T_0 (HJD)	2443091.838(4)	2444450.636(4)	2439175.396(4)
P_{orb} (d)	2.5896870(8)	1.6101553(3)	2.1084195(2)
Light-Time effect			
P_3 (yr)	75(2)	15.1(3)	20.2(2)
T_{per} (HJD)	2679147(7450)	2469052(1315)	2776514(3786)
A_{ETV} (d)	0.044(9)	0.010(2)	0.0081(8)
ω_3 ($^\circ$)	63(29)	317(92)	45(27)
e_3	0.2(1)	0.3(1)	0.4(2)
$f(m_3)$ (M_\odot)	0.082(2)	0.022(1)	0.076(7)
$M_{3,\text{min}}$ (M_\odot)	1.18(1)	0.66(1)	0.34(1)
Mass transfer/loss process			
C_2 ($\times 10^{-10}$ d cycle $^{-1}$)		2.68(2)	19.2(1)
\dot{P} ($\times 10^{-7}$ d yr $^{-1}$)		1.22(1)	6.7(1)
\dot{M}_{tr} ($\times 10^{-8}$ M_\odot yr $^{-1}$)		2.1(5)	4.9(6)
\dot{M}_{loss} ($\times 10^{-7}$ M_\odot yr $^{-1}$)		-1.14(8)	-3.0(2)

several possible mechanisms are given in Table 5 and were calculated using the ‘InPeVEB’ software (Liakos 2015). The upward curvature of the parabola is in good agreement with what would be expected for a conventional semi-detached configuration of this EB. It is a classical Algol system with mass transfer from the less to the more massive component and a rate of $\sim 2.1 \times 10^{-8} M_\odot \text{ yr}^{-1}$. The third body hypothesis suggests a minimum mass of $0.66 M_\odot$ and a potential luminosity contribution of only about $\sim 1.8\%$ in the system (following the formalism of Liakos et al. 2011). This contribution would not have been detectable in the analyses of LCs and RVs.

Most of the eclipse timings for TT Vel were made in the past two decades; after its discovery in 1913, only a few timings were reported in the late 1930s. In the ETV analysis, a parabola fitted the data (Fig. 13-top panel). The residuals indicated a periodic trend, to which a *LITE* curve was fitted (Fig. 13-bottom panel). The orbital period changes agree with a conservative mass transfer from the less to the more massive component of the system with a rate of $\sim 4.9 \times 10^{-8} M_\odot \text{ yr}^{-1}$. The cyclic changes can be explained by the *LITE* that suggests a low mass component ($M_{3,\text{min}} \sim 0.34 M_\odot$), whose light contribution is found less than 0.5% . Therefore, its absence from photometry and spectroscopy is plausible.

5. Pulsation analyses

The oscillation frequencies search was made with the software PERIOD04 v.1.2 (Lenz & Breger 2005), which is based on classical Fourier analysis. Given that the typical frequency range of δ Scuti stars is 4-80 cycle d^{-1} (Breger 2000; Bowman & Kurtz 2018), but as many of them exhibit slower modes (e.g. due to γ Doradus- δ Scuti hybrid nature and/or due to g -mode pulsations), the search was expanded to slower frequency regimes, that is 0-80 cycle d^{-1} . For the analysis of the pulsations, only the best quality ground-based data and the *TESS* data with the best available time resolution were used. For this analysis, the binary model was subtracted from the observed LCs (see Section 3 for details) of each system and the Fourier method on the time-series residuals data was applied. Moreover, since the pulsation amplitudes are modified during the eclipses, and in order to keep an homogeneous data sample, only the out-of-eclipse data points were used. For the three systems, the data corresponding to phases 0.92-0.08 and 0.42-0.58 were excluded.

The S/N of the frequencies was calculated around the area of the signal (Balona 2014) with a spacing of 2 cycle d^{-1} and a box size of 2. A S/N=4, suggested by the developers of the software (see also Breger et al. 1993), as the minimum value of a detected frequency to be considered as reliable was adopted. However, this threshold concerned only the ground-based data sets. For the *TESS* data, based on the conclusions of Baran et al. (2015); Baran & Koen (2021); Bowman & Michielsen (2021), a S/N=5 value was adopted. After the detection of a frequency, the software subtracts it from the observed points and searches for another in the new residuals data until the amplitude of the last frequency reaches the critical S/N.

In Table 6 we list for each observed pass band: the number of nights, the range between the last and the first observed nights, the number of data points, the mean time resolution of these points (δt), the Nyquist frequency (N_{yq}), and the frequency resolution (δf) according to the Rayleigh criterion ($1/\Delta T$). Representative Fourier fittings on the data points of *B* filter (because the maximum amplitude of the pulsations is met in this pass band) and *TESS* (due to their high photometric accuracy) are given for all systems in Fig. 14. The respective periodograms are illustrated in Fig. 15, where the strongest detected frequencies are indicated. The independent pulsation frequencies are listed in Table 7 as follows: the increasing number (n), the value (f_n), the amplitude (A), and the phase (Φ) of each detected frequency that is characterized independent (i.e. it is not a combination of other frequencies). The complete lists of detected frequencies, including also the S/N and the most possible combination of each one, are given in Appendix E for each studied system.

The results from the spectral classification (Section 2.3.1) as well as the frequency regimes where the majority of the frequencies are detected (i.e. 0-4 and 10-40 cycle d^{-1} ; see Tables 7, E.1, E.3, and E.4) suggest clearly that the primaries of the studied systems are pulsating stars of δ Scuti type. The pulsations constant, Q , of the independent frequencies are calculated using the formula of Breger (2000):

$$\log Q = -\log f + 0.5 \log g + 0.1 M_{\text{bol}} + \log T_{\text{eff}} - 6.456, \quad (4)$$

where f is the frequency of the pulsation mode, while $\log g$, M_{bol} , and T_{eff} denote the standard quantities (see Table 4-bottom part). The density of the pulsating star, ρ_{pul} , is calculated with the pulsation constant - density relation:

$$\rho_{\text{pul}}/\rho_\odot = (Q f_{\text{dom}})^2, \quad (5)$$

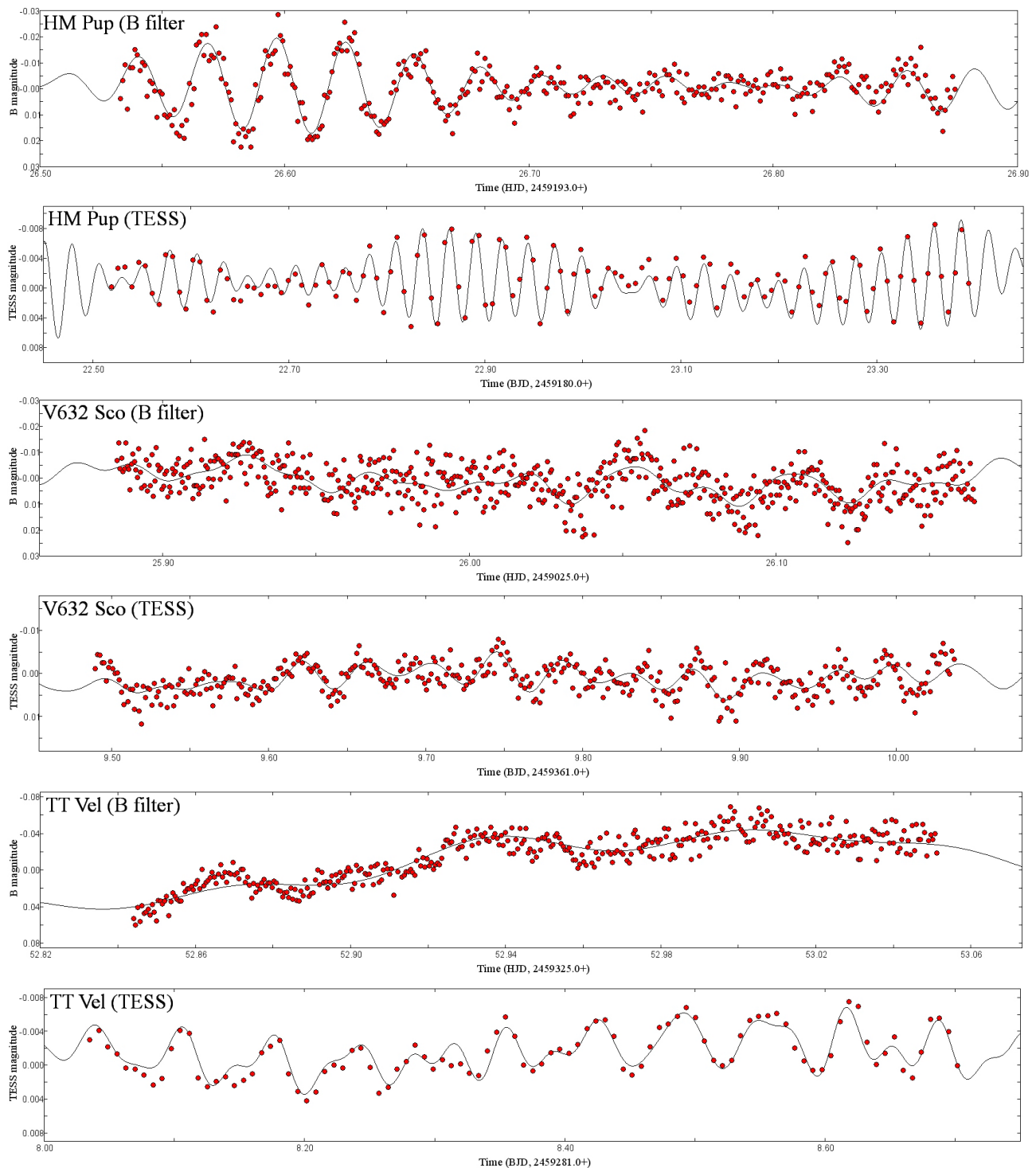


Fig. 14. Representative Fourier fit on the data of *B* filter and *TESS*.

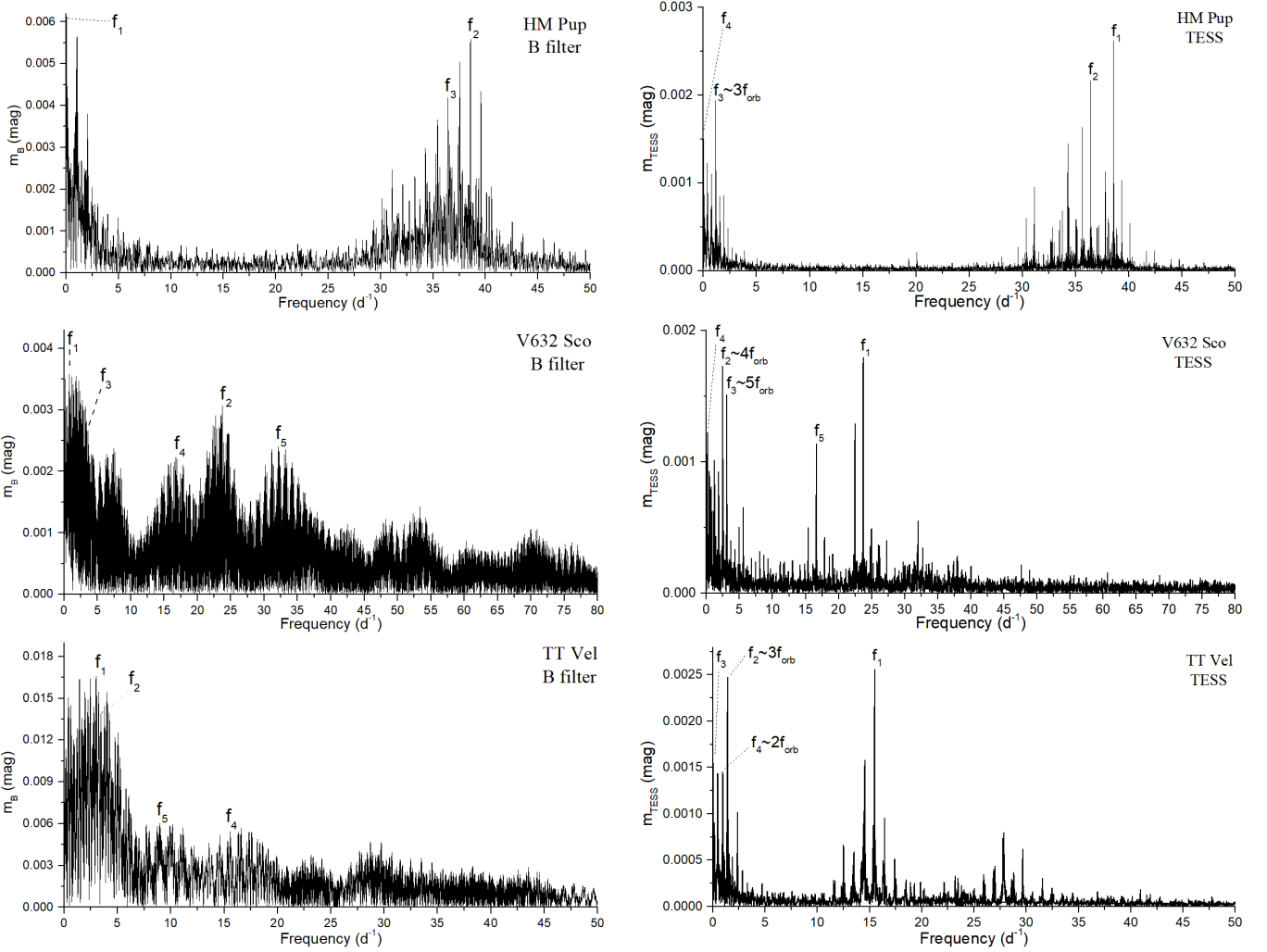
where f_{dom} is the frequency of the dominant pulsation mode. Alternatively, the ρ_{pul} can be also computed using the physical parameters of the stars directly (Table 4), i.e. $\rho_{\text{pul}} = 3M_{\text{pul}}/4\pi R_{\text{pul}}^3$. For the oscillation mode identification, the theoretical MAD models for δ Scuti stars (Montalbán & Dupret 2007) in the FAMIAS software v.1.01 (Zima 2008) were used. Given that for all systems multicolour photometry is available, FAMIAS uses the amplitude and the phase ratios in different filters for a given frequency to estimate the most likely l -degrees based on theoretical models grids. However, it should be noted that, these

models are based on the absolute parameters ($\log g$, M , and T_{eff}) of the pulsators and they have been calculated for single δ Scuti stars. The pulsating stars of the studied systems have increased mass values due to the mass transfer (i.e. their T_{eff} is low for their mass in comparison with main-sequence stars; see Cox 2000), hence, the results for the l degrees can be considered only as approximate.

The following subsections include comments on the analysis and results for each system, while a discussion regarding the real pulsation frequencies is also made. The latter discussion for each system is based on the comparison between the detected

Table 6. Properties of the data sets used for the frequency search.

System	Filter	Nights	ΔT (d)	points	δt (min)	$Nyq.$ (cycle d^{-1})	δf (cycle d^{-1})
HM Pup	<i>B</i>	15	18.3	3678	1.5	494.9	0.054
	<i>V</i>	12	43.2	3168	1.0	701.4	0.023
	<i>I</i>	10	12.2	1893	2.2	472.0	0.082
	<i>TESS</i>	78.2	78.2	6672	10.0	72.04	0.013
V632 Sco	<i>B</i>	8	57.2	2007	0.8	832.6	0.017
	<i>V</i>	2	6.92	335	1.2	1056.4	0.145
	<i>TESS</i>	27.8	27.8	12447	2.0	359.9	0.036
TT Vel	<i>B</i>	16	59.0	1768	0.8	950.4	0.017
	<i>V</i>	12	52.0	232	3.4	101.3	0.019
	<i>I</i>	12	51.3	479	3.4	101.1	0.019
	<i>TESS</i>	24.3	24.3	2060	10.0	72.04	0.041


Fig. 15. Periodograms of *B* filter (left panels) and *TESS* data (right panels). Some of the detected strong frequencies are indicated.

frequencies in the different pass bands of observations. The indices of the compared/discussed frequencies have additionally to their increasing number a filter designation in order to be more easy to be checked by the reader in Tables 7, E.1-E.4. It is quite common in EBs with pulsating components that the imperfect fit of the LCs produces artificial slow frequencies that are connected to instrumental/observational drifts. The time gaps between the ground-based observations may also produce alias frequencies (Breger 2000). Furthermore, searching for pulsations in light curves with eclipses removed also creates aliases at the or-

bitual frequency and multiples thereof. Therefore, distinguishing the real independent frequencies from the possible artefacts is done using the data obtained in bluer pass bands (i.e. *B* and *V*) as indicators for the low-amplitude frequencies (i.e. the pulsations show larger amplitudes in these bands) and the *TESS* data as indicator for the slow frequencies (i.e. no time gaps and higher photometric accuracy). All periodograms were checked for potential sidelobes due to the fast rotation of the pulsating stars (i.e. due to the tidal locking), but none of them showed such evidence. Finally, Table 8 includes the *Q* value and the most possi-

Table 7. Probable independent pulsation frequencies for each observed band.

System	n	f_n (cycle d ⁻¹)	A (mmag)	Φ (°)	
<i>B</i> -filter					
HM Pup	1	0.038(1)	5.9(1)	3(1)	
	2	38.563(1)	5.5(1)	9(1)	
	3	36.424(1)	3.8(1)	354(1)	
	<i>V</i> -filter				
	2	38.563(1)	4.9(1)	14(1)	
	3	36.417(1)	3.7(1)	49(2)	
	5	0.014(1)	2.8(1)	354(3)	
	8	32.806(1)	1.4(1)	88(4)	
	<i>I</i> -filter				
	1	38.562(2)	2.7(1)	15(3)	
	2	36.416(2)	2.4(1)	86(3)	
	<i>TESS</i>				
1	38.5622(1)	2.61(3)	7(1)		
2	36.4196(2)	2.10(3)	14(1)		
4	0.0317(2)	1.92(3)	77(1)		
<i>B</i> -filter					
V632 Sco	1	0.819(1)	3.6(2)	311(4)	
	2	23.539(1)	3.0(2)	141(4)	
	3	3.548(1)	2.3(2)	280(6)	
	4	16.780(1)	2.2(2)	216(6)	
	6	0.216(1)	2.2(2)	21(6)	
	<i>V</i> -filter				
	1	23.432(13)	2.9(5)	81(9)	
	<i>TESS</i>				
	1	23.7423(5)	1.79(4)	134(1)	
	4	0.1746(7)	1.22(4)	230(2)	
	5	16.6507(7)	1.14(4)	205(2)	
	<i>B</i> -filter				
TT Vel	1	3.0101(2)	17.6(4)	96(1)	
	4	15.3267(7)	5.0(4)	171(5)	
	5	8.9257(7)	5.2(4)	137(4)	
	7	16.5918(10)	3.6(4)	151(6)	
	<i>V</i> -filter				
	2	3.5354(5)	10.9(5)	9(3)	
	3	0.7564(7)	7.1(5)	177(4)	
	5	15.7337(14)	3.7(5)	71(7)	
	<i>I</i> -filter				
	1	4.0502(6)	8.7(5)	125(3)	
	2	0.6947(8)	6.6(5)	40(4)	
	3	3.1096(9)	5.7(5)	134(5)	
<i>TESS</i>					
1	15.5020(4)	2.64(5)	36(1)		
3	0.0288(8)	1.36(5)	198(2)		

Notes. The temporal zeropoints for the computation of the phases for each system and per pass-band were: HM Pup: JD2459180.0 (*B*, *V*, *I*) and JD2459193.0 (*TESS*), V632 Sco: JD2459025.0 (*B*, *V*) and JD2459361.0 (*TESS*), and TT Vel: JD2459325.0 (*B*, *V*, *I*) and JD2459281.0 (*TESS*).

ble oscillation mode (l -degrees) for the independent frequencies identified as real as well as the ρ_{pul} of each pulsating star.

5.1. HM Pup

For this system, *B*, *V*, *I*, and *TESS* data were used for the pulsations search. As listed in Table 6, many data points in *B*, *V*, and *I* filters were available; they have a very good time reso-

lution (< 2 min) and cover a time span of more than 40 days. On the other hand, the available *TESS* data have a 10 min time resolution but they cover ~ 78 consecutive days. Moreover, and clearly by chance, the majority of the ground-based observations in *B* and *V* filters and all the data of *I* filter for this system were acquired during the *TESS* observations.

The independent frequencies 38.56 cycle d⁻¹ and 36.42 cycle d⁻¹, as can be seen in Table 7, are detected in all data sets, therefore, they are valid. The $f_{8,V}$ was identified as independent only in *V* filter, while its value is very close to that of $f_{13,B}$, $f_{21,B}$ and $f_{22,T}$ (see Table E.1), thus, probably, it is not an independent frequency. The frequency $f_{5,V}$ was not detected in any of the other filters, therefore, it is probably an artefact. Finally, $f_{1,B}$ and $f_{4,T}$ concern a slow frequency of the order of 0.03 cycle d⁻¹. Although its absence in *V* and *I* filters is spurious, especially since it has the highest amplitude in *B*, we cannot neglect its presence in *TESS* data. Therefore, this frequency can be characterized as suspected-independent frequency. According to the MAD models, the most probable l -degrees for the $f_{2,B}$ ($= f_{1,V}=f_{1,I}=f_{1,T}$) and $f_{3,B}$ ($= f_{2,V}=f_{2,I}=f_{2,T}$) are $l = 2$ and $l = 1$, respectively. The complete list of detected frequencies is given in Table E.1.

5.2. V632 Sco

For the pulsation analysis of V632 Sco we used the short-cadence data set of *TESS* (see Table 2) and only the data set obtained from Congarinni observatory (see Table 1), because it was obtained over a much shorter time period and has higher time resolution in comparison with that obtained from Glen Aplin observatory. Eight nights of observations in *B* filter within a time range of ~ 57 d were available, only two in *V* filter and none in *I* pass band. The *TESS* data cover ~ 28 d of continuous monitoring, therefore, the analysis relies mostly on them.

The frequency ~ 23 cycle d⁻¹ was detected in all data sets, therefore, it is considered as the dominant independent frequency. The second frequency detected both in *B* and *TESS* data is the $f_{4,B}$ ($= f_{5,T}$), thus, we conclude that this is also an independent frequency. The frequency $f_{1,B}$, which is found as the strongest frequency, is not detected in the *TESS* data, therefore its reliability is strongly questioned and it may be attributed to instrumental/observational drifts or imperfect LC fitting. The frequency $f_{3,B}$ is close to the value of $6f_{\text{orb}}$ ($=3.726$ cycle d⁻¹) but it can also be the alias frequency of ~ 2.548 cycle d⁻¹ (i.e. $f_{3,B}-1$), which is found as $f_{2,T}$ ($= 4f_{\text{orb}}$). So, this frequency can be considered only as a suspected independent frequency. Similar to that found for HM Pup, a slow frequency is detected in *B* and *TESS* data (i.e. $f_{6,B}$ and $f_{4,T}$), and it is of the order of 0.2 cycle d⁻¹. Although $f_{6,B}$ and $f_{4,T}$ have relatively similar values, it cannot be concluded that this frequency is indeed independent. In conclusion, $f_{2,B}$ ($= f_{1,V} = f_{1,T}$) and $f_{4,B}$ ($= f_{5,T}$) are certainly the dominant and independent frequencies of the pulsating star of V632 Sco. It should be noted that the ground-based and the *TESS* observations have a time difference of approximately 11 months. Thus, for the l -degrees calculation of the first independent frequency, i.e. $f_{2,B}$, the amplitude and phase ratios of the *B* and *V* filter sets were used. Moreover, $f_{4,B}$ was not detected in the *V*-filter data set. Therefore, for the l -degrees of the second independent frequency, we assumed that a) no modulation in the amplitude and phase of this frequency was made within these 11 months and b) the amplitude of a frequency in *TESS* pass-band is similar to that of the *I* filter. The latter assumption can be supported by the similarity of the wavelength coverage of *TESS* (i.e. 600-1000 nm, with a peak at ~ 880 nm; Ricker et al. 2015) and that of the *I* filter (i.e. 720-850 nm, with a peak at

Table 8. Independent pulsation frequencies and MAD model results for the δ Scuti stars in each system.

f (d^{-1})	A_B (mmag)	Q (d)	l -deg.	ρ (ρ_\odot)
HM Pup				
38.563(1)	5.5(1)	0.012(1)	2	0.21(3) ^a /0.19(1) ^b
36.424(1)	3.8(1)	0.017(1)	1	
V632 Sco				
23.539(1)	3.0(2)	0.018(2)	3 or 1	0.18(3) ^a /0.18(1) ^b
16.780(1)	2.2(2)	0.025(3)	2 or 3	
TT Vel				
15.327(1)	5.0(4)	0.030(3)	3	0.21(3) ^a /0.21(1) ^b

Notes. ^aBased on Eq. 5, ^bbased on the physical properties of stars (Table 4).

~ 790 nm; Ricker et al. 2015) and can be checked also in the results of HM Pup (Table E.2) for the I filter and $TESS$ data sets. Finally, based on MAD models and the aforementioned assumptions, the l -degrees are estimated as 3 or 1 for the $f_{2,B}$ and 2 or 3 for $f_{4,B}$. In total, 11 frequencies were detected in B filter and 12 in the $TESS$ data (Table E.3).

5.3. TT Vel

In the search for frequencies of pulsations in TT Vel, we relied mostly on only good ground-based B data set and the mid-cadence data set of $TESS$. Some observations through the V and I filters were obtained, but were spread over a 50 day time-period (see Table 7). However, for reasons of clarity, a frequency search was also made on these data sets.

Four possible independent frequencies were detected in B filter (Table 8). The frequency $f_{4,B}$ is the same with $f_{5,V}$ and $f_{1,T}$ and can be plausibly considered as the dominant frequency in the δ Scuti regime. $f_{5,B}$ and $f_{7,B}$ are again in the frequency range of δ Scuti stars, but they are not found in all filters. The frequencies $f_{1,B}$, $f_{1,T}$, and $f_{3,T}$ are slow frequencies and cannot be verified as real ones. The remaining frequencies in V filter and all frequencies in I filter are not very reliable because of the poor data sets used.

Eight and 19 frequencies were detected in the B and $TESS$ data sets, respectively (Table E.4). However, only the $f \sim 15$ cycle d^{-1} is definitely an independent frequency. It should be noted that since the ground-based and the $TESS$ observations were made within a time range of approximately 100 days, we assumed that the phase and the amplitude of this frequency remained constant, and the result of the MAD models is $l = 3$.

The independent frequencies of the pulsating primary component of each system are shown in Table 8, where A_B is the amplitude in the B band, Q is the pulsation constant and ρ the density of the pulsator. Based on these Q values and the models of Fitch (1981, $M = 2 M_\odot$ for HM Pup and V632 Sco and $M = 1.5 M_\odot$ for TT Vel), these frequencies are identified as non-radial pressure oscillation modes. Moreover, all of them, except the $f = 38.563$ cycle d^{-1} of HM Pup, have typical Q values for δ Scuti stars ($0.015 < Q < 0.035$; Breger 2000).

6. Evolution and comparison with similar systems

The positions of the components of HM Pup, V632 Sco and TT Vel on the mass-radius ($M - R$) and Hertzsprung-Russell

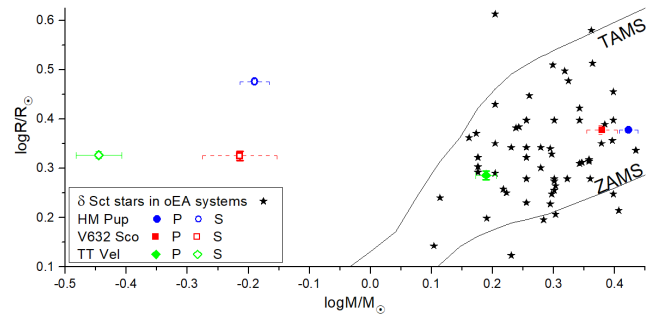


Fig. 16. Location of the primary (filled symbols) and secondary (empty symbols) components of HM Pup (points), V632 Sco (squares), and TT Vel (diamonds) within the mass-radius diagram. The stars symbols denote the δ Scuti components of other oEA systems (taken from Liakos & Niarchos 2017), while the black solid lines represent the boundaries of main-sequence.

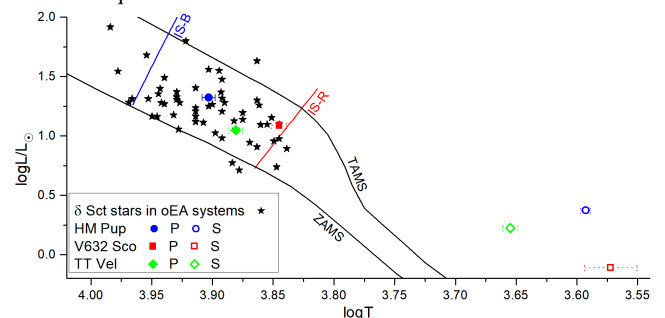


Fig. 17. Location of the components of the studied systems within the HR diagram. Symbols and black solid lines have the same meaning as in Fig. 16. The coloured solid lines (B=Blue, R=Red) denote the boundaries of the instability strip (IS; taken from Murphy et al. 2019).

(HR) evolutionary diagrams are shown in Figs 16 and 17, respectively. The locations of their primaries relative to pulsating components of other oEA stars in the relationship between pulsation and orbital periods ($P_{orb} - P_{pul}$) are shown in Fig. 18. The locations of the same components in the relationship between the pulsation periods and stellar gravity $\log g - P_{pul}$ are shown in Fig. 19 (c.f. Liakos & Niarchos 2017; Liakos 2017). The data points for these diagrams were collected from Liakos & Niarchos (2017, Table 1 therein) and the online catalogue⁸ of these systems (detailed lists will be published in a future study).

The primary components of each system lie in the centre of the main-sequence within the instability strip (Fig. 17). The evolution of Algol binary systems, in which mass ratio reversal occurs, is complex and is not an aim for discussion in this paper. The primary component of V632 Sco is close to the red edge of the instability strip and the border with the γ Doradus stars (Uytterhoeven et al. 2011). This evolutionary position, together with the frequency analysis indicating a probable independent frequency in the 0-4 cycle d^{-1} range (Section 5.2), suggests that this star could have a δ Scuti- γ Doradus hybrid nature.

There is a relationship between the frequency of pulsations and orbital period in close binary systems (c.f. Liakos & Niarchos 2017). The primary components of V632 Sco and TT Vel fit the trend calculated by Liakos & Niarchos (2017) quite well, whereas that of HM Pup deviates a little from it (Fig. 18). Furthermore, a relationship has been found between the pulsation period and the evolutionary stage ($\log g$) of the δ Scuti-type components of close binary stars (Liakos & Niarchos 2017), although it is based on only a small sample of systems where radial

⁸ <http://alexiosliakos.weebly.com/catalogue.html>

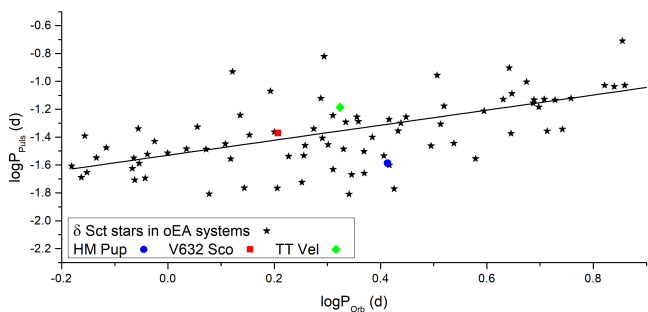


Fig. 18. Locations of the pulsating components of each studied system and other δ Scuti stars-members of oEA stars within the $P_{\text{orb}}-P_{\text{pul}}$ diagram. Symbols have the same meaning as in Fig. 16, while the solid line denotes the empirical fit of Liakos & Niarchos (2017).

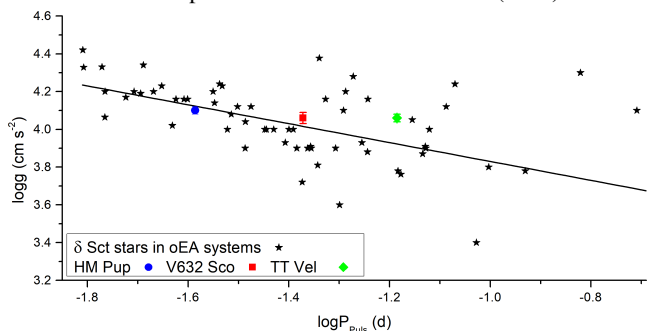


Fig. 19. Locations of the pulsating components of each studied system and other δ Scuti stars-members of oEA stars within the $\log g-P_{\text{pul}}$ diagram. Symbols and line have the same meaning as in Fig. 18.

velocities have been determined. The primaries of HM Pup and V632 Sco are very close to the empirical fit, while that of TT Vel shows larger deviation.

The secondary components of each system are well above terminal age on the Main Sequence (Figs. 16 and 17). Their derived $\log g$ values are 3.3-3.57 cm s^{-2} (Table 4), which indicate all of them are in the subgiant/giant evolutionary phase of evolution. As the primary eclipse of HM Pup is total, we were able to observe and classify the spectrum of its secondary component and confirm that it is a subgiant or giant, although smaller in size than typical single giant K8 stars.

7. Summary and conclusions

In this study we present a holistic and detailed analysis of three southern EBs with a pulsating component. Multi-filter ground-based photometric observations and *TESS* data were used. Moreover, spectroscopic observations were obtained allowing for the determination of the spectral types of the primaries of all systems and the secondary of HM Pup as well as the RVs of both components. The combination of these data provided the means for accurate photometric modelling followed by the determination of the physical parameters and the evolutionary stages of the components of the systems. Analysis of eclipse timings collected from the literature, and our observations, offered the opportunity to determine possible orbital period modulation mechanisms and quantify the mass transfer/loss rates, which were found in the spectra. The residuals of the LCs were analysed to detect pulsation frequencies. The frequencies detected in different wavelength bands were compared with each other in order to determine the oscillation modes of the pulsators. The primary components of the systems were identified as δ Scuti type stars based on their physical (i.e. T_{eff} , M , and R) and pulsation properties (fre-

quency ranges). All systems were found to be in a semi-detached configuration with the primaries being main-sequence stars and with the secondaries (cooler and less massive components) filling their Roche lobes and being in evolved evolutionary stages. Therefore, these systems are classical Algols (in terms of evolution) and are oEA stars according to the definition of Mkrtichian et al. (2002). The current status of these systems confirm the conclusion of Liakos & Niarchos (2017) regarding the earlier initiation of the pulsations due to the presence of a close companion.

The primary component of HM Pup pulsates in two independent frequencies at 36.4 and 38.6 cycle d^{-1} , which are identified as p -mode oscillations. In total, 22 and 26 frequencies were detected in *B* filter and *TESS* data, respectively, but all except the two above are combinations of other frequencies. The HM Pup orbital period has one cyclic variation which cannot be fully explained by the possible presence of a tertiary companion. No third light trace was detected in the analyses of light curves, Na I D spectra and broadening function values. On the other hand, our results show there is evidence for gas streaming from the secondary component and impacting on the primary component. The secondary component was found to be magnetically active and at a subgiant-giant phase of evolution.

The pulsating component of V632 Sco oscillates in two independent frequencies at 23.54 and 16.78 cycle d^{-1} , which are independent non-radial pressure mode oscillations. More frequencies were detected (11 and 12 in the *B* filter and *TESS* data, respectively), but they are combinations of others. Another one was found in the slow-frequency regime, but its value was not exactly the same in all data sets, therefore, it might be an artefact. On the other hand, the location of the primary-pulsating component on the borders of δ Scuti- γ Doradus stars leaves open the possibility of an hybrid nature. The secular changes in the orbital period of the system indicate a mass transfer from the secondary component at the rate of $2.1 \times 10^{-8} M_{\odot} \text{yr}^{-1}$. As is the case for all three systems, mass flow from the secondary component is seen in the sodium doublet spectra. Furthermore, there is no evidence of a tertiary component in the sodium spectra, nor in the broadening function analyses. The secondary component was found to have an active spot migrating with a time period of a few days.

For the δ Scuti star of TT Vel at least seven frequencies were detected in *B*, *V*, and *I* filters and more than 15 in the *TESS* data. However, only one ($\sim 15.3 \text{ cycle d}^{-1}$) was validated as a real independent frequency and is identified as a p -mode oscillation. The other potential independent frequencies were either not detected in all data sets or they are combinations of other frequencies. The secular changes of the orbital period can be explained with a mass transfer rate of $4.9 \times 10^{-8} M_{\odot} \text{yr}^{-1}$. However, the current evolutionary status of the components gives rise to the possibility of mass loss from the system. The mass loss was calculated as $-3 \times 10^{-7} M_{\odot} \text{yr}^{-1}$, and probably both mechanisms occur with slower rates. The periodic changes of the orbital period might be due to the presence of a faint tertiary component.

More studies of similar systems will enrich the sample of oEA stars with accurately determined absolute properties, which in turn, will improve knowledge of how interactions of components in close binary systems influence pulsations.

Acknowledgements. AL acknowledges financial support by the European Space Agency (ESA) under the Consolidating Activities Regarding Moon, Earth and NEOs (CARMEN) project, NOA/SRFA no. 1084 and wishes to thank Dr N. Nanouris for his valuable comments on the ETV analysis. DJWM, MGB and JFW acknowledge grants for time on the ANU 2.3 m telescope from the Edward Corbould Research Fund of the Astronomical Association of Queensland. DJWM is grateful to Prof. Michael Drinkwater for his extensive assistance with the planning and data analysis of the ANU 2.3 m telescope obser-

vations. DJWM thanks A. Mohit, Y. Rist and L. Coetzee for their assistance with the spectroscopic observations. We thank the anonymous reviewer for the valuable comments that improved the quality of this work. This research has made use of NASA's Astrophysics Data System Bibliographic Services, the SIMBAD database, operated at CDS, Strasbourg, France, the TIDAK database (B. Zakrzewski), the 'O-C' gateway database, and the Mikulski Archive for Space Telescopes (MAST).

References

- Aerts, C., Christensen-Dalsgaard, J., & Kurtz, D. W. 2010, *Asteroseismology* (Springer Netherlands)
- Antoci, V., Cunha, M., Houdek, G., et al. 2014, *ApJ*, 796, 118
- Applegate, J. H. 1992, *ApJ*, 385, 621
- Applegate, J. H. & Patterson, J. 1987, *ApJ*, 322, L99
- Balona, L. A. 2014, *MNRAS*, 439, 3453
- Balona, L. A., Daszyńska-Daszkiewicz, J., & Pamyatnykh, A. A. 2015, *MNRAS*, 452, 3073
- Baran, A. S. & Koen, C. 2021, *Acta Astron.*, 71, 113
- Baran, A. S., Koen, C., & Pokrzywka, B. 2015, *MNRAS*, 448, L16
- Berdyugina, S. V. 2005, *Living Reviews in Solar Physics*, 2, 8
- Borucki, W. J., Koch, D., Basri, G., et al. 2010, *Science*, 327, 977
- Bowman, D. M., Johnston, C., Tkachenko, A., et al. 2019, *ApJ*, 883, L26
- Bowman, D. M. & Kurtz, D. W. 2018, *MNRAS*, 476, 3169
- Bowman, D. M. & Michielsen, M. 2021, *A&A*, 656, A158
- Breger, M. 2000, in *Astronomical Society of the Pacific Conference Series*, Vol. 210, *Delta Scuti and Related Stars*, ed. M. Breger & M. Montgomery, 3
- Breger, M., Stich, J., Garrido, R., et al. 1993, *A&A*, 271, 482
- Claret, A. 2018, *A&A*, 618, A20
- Coelho, P., Barbuy, B., Meléndez, J., Schiavon, R. P., & Castilho, B. V. 2005, *A&A*, 443, 735
- Collins, K. A., Kielkopf, J. F., Stassun, K. G., & Hessman, F. V. 2017, *AJ*, 153, 77
- Cox, A. N. 2000, *Allen's astrophysical quantities* (New York: Springer-Verlag)
- Dopita, M., Hart, J., McGregor, P., et al. 2007, *Ap&SS*, 310, 255
- Dopita, M., Rhee, J., Farage, C., et al. 2010, *Ap&SS*, 327, 245
- Drake, A. J., Djorgovski, S. G., Mahabal, A., et al. 2009, *ApJ*, 696, 870
- Fitch, W. S. 1981, *ApJ*, 249, 218
- Gray, R. O. & Corbally, C. J. 2014, *AJ*, 147, 80
- Gray, R. O. & Corbally, Christopher, J. 2009, *Stellar Spectral Classification* (Princeton University Press)
- Handler, G. 1999, *MNRAS*, 309, L19
- Henden, A. A., Levine, S., Terrell, D., & Welch, D. L. 2015, in *American Astronomical Society Meeting Abstracts*, Vol. 225, *American Astronomical Society Meeting Abstracts #225*, 336.16
- Hilditch, R. W. 2001, *An Introduction to Close Binary Stars* (Cambridge University Press)
- Hoffman, D. I., Harrison, T. E., McNamara, B. J., et al. 2006, *AJ*, 132, 2260
- Howell, S. B., Sobeck, C., Haas, M., et al. 2014, *PASP*, 126, 398
- Irwin, J. B. 1959, *AJ*, 64, 149
- Kalimeris, A., Rovithis-Livanou, H., & Rovithis, P. 1994, *A&A*, 282, 775
- Kim, S.-L., Lee, J. W., Lee, C.-U., et al. 2021, *AJ*, 162, 212
- Koch, D. G., Borucki, W. J., Basri, G., et al. 2010, *ApJ*, 713, L79
- Kruszewski, A. 1966, *Advances in Astronomy and Astrophysics*, 4, 233
- Kurtz, D. W., Handler, G., Rappaport, S. A., et al. 2020, *MNRAS*[arXiv:2004.03471]
- Lanza, A. F. 2006, *MNRAS*, 369, 1773
- Lanza, A. F. 2020, *MNRAS*, 491, 1820
- Lanza, A. F., Catalano, S., Cutispoto, G., Pagano, I., & Rodono, M. 1998, *A&A*, 332, 541
- Lanza, A. F. & Rodonò, M. 2002, *Astronomische Nachrichten*, 323, 424
- Lenz, P. & Breger, M. 2005, *Communications in Asteroseismology*, 146, 53
- Liakos, A. 2015, in *Astronomical Society of the Pacific Conference Series*, Vol. 496, *Living Together: Planets, Host Stars and Binaries*, ed. S. M. Rucinski, G. Torres, & M. Zejda, 286
- Liakos, A. 2017, *A&A*, 607, A85
- Liakos, A. 2018, *A&A*, 616, A130
- Liakos, A. 2020a, *A&A*, 642, A91
- Liakos, A. 2020b, *Acta Astron.*, 70, 265
- Liakos, A. & Cagaš, P. 2014, *Ap&SS*, 353, 559
- Liakos, A. & Niarchos, P. 2013, *Ap&SS*, 343, 123
- Liakos, A. & Niarchos, P. 2017, *MNRAS*, 465, 1181
- Liakos, A. & Niarchos, P. 2020, *Galaxies*, 8, 75
- Liakos, A., Niarchos, P., Soydogan, E., & Zasche, P. 2012, *MNRAS*, 422, 1250
- Liakos, A., Zasche, P., & Niarchos, P. 2011, *New A*, 16, 530
- Lucy, L. B. 1967, *ZAp*, 65, 89
- Mkrtychian, D. E., Gunsriwivat, K., Reichart, D. E., et al. 2018a, *Information Bulletin on Variable Stars*, 6238, 1
- Mkrtychian, D. E., Kusakin, A. V., Gamarova, A. Y., & Nazarenko, V. 2002, in *Astronomical Society of the Pacific Conference Series*, Vol. 259, *IAU Colloq. 185: Radial and Nonradial Pulsations as Probes of Stellar Physics*, ed. C. Aerts, T. R. Bedding, & J. Christensen-Dalsgaard, 96
- Mkrtychian, D. E., Lehmann, H., Rodríguez, E., et al. 2018b, *MNRAS*, 475, 4745
- Montalbán, J. & Dupret, M. A. 2007, *A&A*, 470, 991
- Moriarty, D. J. W., Bohlens, T., Heathcote, B., Richards, T., & Streamer, M. 2013, *Journal of the American Association of Variable Star Observers (JAAVSO)*, 41, 182
- Moriarty, D. J. W., Liakos, A., Drinkwater, M. J., et al. 2019, *Ap&SS*, 365, 1
- Murphy, S. J., Hey, D., Van Reeth, T., & Bedding, T. R. 2019, *MNRAS*, 485, 2380
- Murphy, S. J., Pigulski, A., Kurtz, D. W., et al. 2013, *MNRAS*, 432, 2284
- Nelson, Robert, H. 2005, *B-Minima*
- Ogloza, W., Stachowski, G., Zakrzewski, B., & Zejmo, M. 2022, in *XL Polish Astronomical Society Meeting proc*, Vol. 123, *XL Polish Astronomical Society Meeting*, in press
- Pilecki, B., Gieren, W., Smolec, R., et al. 2017, *ApJ*, 842, 110
- Pojmanski, G. 2002, *Acta Astron.*, 52, 397
- Prša, A. & Zwitter, T. 2005, *ApJ*, 628, 426
- Richards, M. T. & Albright, G. E. 1999, *ApJS*, 123, 537
- Ricker, G. R., Latham, D. W., Vanderspek, R. K., et al. 2009, in *American Astronomical Society Meeting Abstracts*, Vol. 213, *American Astronomical Society Meeting Abstracts #213*, 403.01
- Ricker, G. R., Winn, J. N., Vanderspek, R., et al. 2015, *Journal of Astronomical Telescopes, Instruments, and Systems*, 1, 014003
- Rovithis-Livanou, H., Kranidiotis, A. N., Rovithis, P., & Athanassiades, G. 2000, *A&A*, 354, 904
- Ruciński, S. M. 1969, *Acta Astron.*, 19, 245
- Ruciński, S. M. 1992, *AJ*, 104, 1968
- Ruciński, S. M. 2002, *AJ*, 124, 1746
- Shappee, B., Prieto, J., Stanek, K. Z., et al. 2014, in *American Astronomical Society Meeting Abstracts*, Vol. 223, *American Astronomical Society Meeting Abstracts #223*, 236.03
- Soydogan, F., Soydogan, E., Kanvermez, Ç., & Liakos, A. 2013, *MNRAS*, 432, 3278
- Stassun, K. G., Oelkers, R. J., Paegert, M., et al. 2019, *AJ*, 158, 138
- Streamer, M., Bohlens, T., & Ogmen, Y. 2016, *Journal of the American Association of Variable Star Observers (JAAVSO)*, 44, 39
- Ulaş, B., Gazeas, K., Liakos, A., et al. 2020, *Acta Astron.*, 70, 219
- Uytterhoeven, K., Moya, A., Grigahcène, A., et al. 2011, *A&A*, 534, A125
- van Hamme, W. 1993, *AJ*, 106, 2096
- Völschow, M., Schleicher, D. R. G., Banerjee, R., & Schmitt, J. H. M. M. 2018, *A&A*, 620, A42
- von Zeipel, H. 1924, *MNRAS*, 84, 665
- Wilson, R. E. 1979, *ApJ*, 234, 1054
- Wilson, R. E. 1990, *ApJ*, 356, 613
- Wilson, R. E. & Devinney, E. J. 1971, *ApJ*, 166, 605
- Zasche, P., Liakos, A., Niarchos, P., et al. 2009, *New A*, 14, 121
- Zima, W. 2008, *Communications in Asteroseismology*, 157, 387

Appendix A: Radial velocities

This appendix includes the heliocentric radial velocities measurements of the studied systems. In Table A.1 we list: the heliocentric Julian date of the observations and the radial velocities of the components of the systems (1=primary, 2=secondary). Details regarding the calculation method of the RVs are given in Section 3.

Table A.1. Radial velocities measurements.

HJD-2450000	RV_1 (km s ⁻¹)	RV_2 (km s ⁻¹)	HJD-2450000	RV_1 (km s ⁻¹)	RV_2 (km s ⁻¹)	HJD-2450000	RV_1 (km s ⁻¹)	RV_2 (km s ⁻¹)
HM Pup			9360.8937	17(5)	251(13)	9301.8991	61(6)	-148(10)
7798.0305	94(5)	-147(13)	9361.8788	89(5)	-66(13)	9301.9506	60(6)	-151(10)
7798.0371	96(5)	-141(13)	9361.8833	96(5)	-55(13)	9301.9822	62(6)	-156(10)
7798.0445	104(5)	-146(13)	9361.8878	97(5)	-57(13)	9302.0427	66(6)	-150(10)
7798.0469	99(5)	-124(13)	V632 Sco			9302.0902	57(6)	-148(10)
7889.9488	21(5)	256(13)	8241.1658	37(9)	-217(14)	9305.0406	-11(6)	185(10)
7889.9519	23(5)	257(13)	8241.1973	36(9)	-211(14)	9305.0483	-15(6)	177(10)
7889.9550	18(5)	234(13)	8241.2025	43(9)	-200(14)	9305.0856	-20(6)	188(10)
7889.9590	18(5)	238(13)	8241.2129	34(9)	-218(14)	9305.0894	-20(6)	186(10)
7916.8682	92(5)	-105(13)	8270.0536	20(9)	-199(14)	9305.0932	-14(6)	195(10)
8240.8736	109(5)	-119(13)	8270.2046	32(9)	-222(14)	9305.1232	-17(6)	194(10)
8240.8788	111(5)	-143(13)	8270.9209	-62(9)	194(14)	9305.1308	-16(6)	196(10)
8240.8840	105(5)	-115(13)	8270.9864	-67(9)	168(14)	9360.8630	58(6)	-111(10)
8270.8744	15(5)	211(13)	8270.9911	-70(9)	168(14)	9360.8661	59(6)	-107(10)
8924.8909	89(5)	-83(13)	8270.9956	-75(9)	168(14)	9360.8692	58(6)	-122(10)
8924.8934	82(5)	-61(13)	8271.0203	-74(9)	170(14)	9360.9579	68(6)	-130(10)
9155.1041	107(5)	-113(13)	8271.1079	-79(9)	180(14)	9360.9611	72(6)	-137(10)
9155.1093	106(5)	-114(13)	8271.1138	-78(9)	191(14)	9360.9725	74(6)	-126(10)
9156.1914	13(5)	213(13)	8271.1190	-80(9)	190(14)	9361.8664	-11(6)	151(10)
9156.2005	11(5)	218(13)	9034.1377	-44(9)	194(14)	9361.8695	-6(6)	145(10)
9184.9968	15(5)	235(13)	9034.1429	-44(9)	194(14)	9361.8726	-8(6)	155(10)
9185.0934	20(5)	190(13)	9038.0233	-55(9)	146(14)	9362.9335	60(6)	-109(10)
9186.0966	102(5)	-113(13)	9038.9285	-53(9)	156(14)	9362.9380	65(6)	-101(10)
9186.1297	100(5)	-134(13)	9038.9337	-62(9)	156(14)	9362.9426	61(6)	-112(10)
9329.8694	11(5)	234(13)	9038.9803	-65(9)	184(14)	9362.9504	56(6)	-115(10)
9329.8732	15(5)	244(13)	9038.9855	-60(9)	160(14)	9362.9549	56(6)	-121(10)
9329.8770	13(5)	250(13)	9039.1021	-69(9)	179(14)	9362.9653	50(6)	-126(10)
9330.8914	101(5)	-109(13)	9039.1073	-63(9)	193(14)	9362.9705	50(6)	-125(10)
9330.8959	105(5)	-98(13)	TT Vel			9362.9757	53(6)	-134(10)
9330.9790	97(5)	-114(13)	9185.1077	-6(6)	168(10)	9362.9811	52(6)	-132(10)
9330.9822	106(5)	-113(13)	9185.1182	-9(6)	190(10)	9362.9863	51(6)	-140(10)
9360.8861	15(5)	225(13)	9185.1213	-8(6)	185(10)			
9360.8899	14(5)	258(13)	9186.1031	55(6)	-159(10)			

Appendix B: Gas velocities of HM Pup

This appendix (Table B.1) includes for various orbital phases of HM Pup the velocities of the primary component (V_1), based on the centered wavelength (λ_1) of its Na I D line, the centered wavelength of the line of the gas (λ_{gas}), and its corresponding velocity (V_{gas}) as well as the relative velocity of the gas to the primary component ($V_{1, \text{gas}}$). The wavelengths and velocities were adjusted, for clarity, to remove the fixed systemic velocity of 58 km s⁻¹.

Table B.1. Velocities of the HM Pup primary star and wavelengths and velocities of its Na I D lines and the gas stream from the secondary star at a range of orbital phases (with systemic velocity subtracted).

Phase	V_1 (km s ⁻¹)	λ_1 (Å)	λ_{gas} (Å)	V_{gas} (km s ⁻¹)	$V_{1, \text{gas}}$ (km s ⁻¹)	Phase	V_1 (km s ⁻¹)	λ_1 (Å)	λ_{gas} (Å)	V_{gas} (km s ⁻¹)	$V_{1, \text{gas}}$ (km s ⁻¹)
0.24	-44.91	5890.23	5890.50	-31.02	13.89	0.62	30.80	5891.71	5890.68	-21.86	-52.67
0.28	-44.20	5890.24	5890.68	-21.86	22.34	0.66	37.99	5891.86	5890.60	-25.93	-63.93
0.32	-40.72	5890.31	5890.30	-41.20	-0.49	0.75	45.00	5891.99	5890.40	-36.11	-81.11
0.35	-36.41	5890.39	5889.86	-63.60	-27.19	0.77	44.65	5891.99	5890.28	-42.22	-86.87
0.42	-21.68	5890.68	5890.28	-42.22	-20.54	0.88	30.80	5891.71	5890.50	-31.02	-61.83
0.50	0.00	5891.11	5890.50	-31.02	-31.02						

Appendix C: Spots

The location of the spots on the secondary components of the systems, assumed in the LCs and RVs modelling (Section 3), are given in Table C.1. This table lists: The pass bands used for modelling LCs and RVs, the number of spots for each model, and the parameters of the spots (Co-latitude, longitude, radius, and temperature factor). The letter ‘G’ given for the models of V632 Sco using the *TESS* data stands for group of LCs (see Section 3 for details).

Table C.1. Spot location on the surface of the secondary components.

Filters	HM Pup			TT Vel			V632 Sco		
	<i>BVI</i>	<i>TESS</i>		<i>TESS</i>	<i>B</i>	<i>VI</i>	<i>TESS – G1</i>	<i>TESS – G2</i>	<i>TESS – G3</i>
Spot	1	1	2	1	1	1	1	1	1
<i>Co – latitude</i> (°)	59(4)	57(4)	62(4)	111(15)	84(9)	81(10)	73(5)	68(4)	67(5)
<i>Longitude</i> (°)	59(4)	52(4)	225(4)	262(8)	329(2)	90(13)	259(2)	261(2)	260(3)
<i>Radius</i> (°)	26(3)	30(3)	16(4)	11(2)	20(1)	17(2)	24(1)	26(1)	27(1)
T_f ($T_{\text{spot}}/T_{\text{sur}}$)	0.8(1)	0.9(1)	1.1(1)	0.7(1)	0.7(1)	0.8(1)	0.7(1)	0.8(1)	0.8(1)

Notes. G=Group of LCs, T_{spot} =temperature of the spot, T_{sur} =temperature of the surface

Appendix D: Times of minima

Table D.1 hosts the times of minima calculated from personal ground-based observations and the available data from the *TESS* mission. We list: the heliocentric Julian date and the type (I=primary eclipse, II=secondary eclipse) of each minimum and the filters used for the individual observations. In cases where two or more filters are listed for a given minimum time, the latter is the average of the times of minima calculated for the data of each filter. More details about the calculation method are given in Section 4.

Table D.1. Times of minima derived from the ground-based and *TESS* data.

HJD	Type	Filter	HJD	Type	Filter	HJD	Type	Filter
HM Pup			2459203.6011(5)	II	<i>TESS</i>	2459250.2161(4)	II	<i>TESS</i>
2458492.7218(17)	I	<i>TESS</i>	2459204.8999(1)	I	<i>TESS</i>	2459251.5152(1)	I	<i>TESS</i>
2458494.0194(11)	II	<i>TESS</i>	2459206.1902(11)	II	<i>TESS</i>	2459252.8054(7)	II	<i>TESS</i>
2458495.3100(15)	I	<i>TESS</i>	2459207.4897(1)	I	<i>TESS</i>	2459256.6947(1)	I	<i>TESS</i>
2458496.6085(4)	II	<i>TESS</i>	2459208.7809(7)	II	<i>TESS</i>	2459257.9845(6)	II	<i>TESS</i>
2458497.9042(65)	I	<i>TESS</i>	2459210.0794(1)	I	<i>TESS</i>	2459259.2844(1)	I	<i>TESS</i>
2458499.1989(3)	II	<i>TESS</i>	2459211.3700(5)	II	<i>TESS</i>	2459260.5742(10)	II	<i>TESS</i>
2458500.4906(14)	I	<i>TESS</i>	2459212.6691(1)	I	<i>TESS</i>	2459261.8741(1)	I	<i>TESS</i>
2458501.7885(11)	II	<i>TESS</i>	2459216.5486(6)	II	<i>TESS</i>	2459263.1644(13)	II	<i>TESS</i>
2458505.6704(37)	I	<i>TESS</i>	2459217.8487(1)	I	<i>TESS</i>	2459264.4639(1)	I	<i>TESS</i>
2458506.9692(8)	II	<i>TESS</i>	2459220.4383(1)	I	<i>TESS</i>	2459265.7524(9)	II	<i>TESS</i>
2458508.2595(18)	I	<i>TESS</i>	2459221.7283(6)	II	<i>TESS</i>	2459273.5229(9)	II	<i>TESS</i>
2458509.5573(7)	II	<i>TESS</i>	2459221.7288(2)	II	<i>V, I</i>	2459274.8228(1)	I	<i>TESS</i>
2458510.8518(71)	I	<i>TESS</i>	2459223.0281(1)	I	<i>TESS</i>	2459276.1122(8)	II	<i>TESS</i>
2458512.1472(5)	II	<i>TESS</i>	2459224.3191(12)	II	<i>TESS</i>	2459277.4126(1)	I	<i>TESS</i>
2458513.4389(23)	I	<i>TESS</i>	2459225.6171(1)	I	<i>I</i>	2459278.7033(9)	II	<i>TESS</i>
2458514.7366(4)	II	<i>TESS</i>	2459225.6178(1)	I	<i>TESS</i>	V632 Sco		
2458518.6191(2)	I	<i>TESS</i>	2459226.9085(7)	II	<i>TESS</i>	2458285.1077(30)	I	<i>B, V, I</i>
2458519.9167(16)	II	<i>TESS</i>	2459229.4972(6)	II	<i>TESS</i>	2458625.6675(85)	II	<i>TESS</i>
2458521.2091(8)	I	<i>TESS</i>	2459230.7967(21)	I	<i>I</i>	2458626.4660(6)	I	<i>TESS</i>
2458522.5059(3)	II	<i>TESS</i>	2459230.7973(1)	I	<i>TESS</i>	2458628.0767(4)	I	<i>TESS</i>
2458523.7989(19)	I	<i>TESS</i>	2459232.0874(4)	II	<i>TESS</i>	2458628.8809(29)	II	<i>TESS</i>
2458526.3884(1)	I	<i>TESS</i>	2459233.3870(1)	I	<i>TESS</i>	2458629.6863(1)	I	<i>TESS</i>
2458527.6862(10)	II	<i>TESS</i>	2459234.6758(6)	II	<i>TESS</i>	2458631.2966(2)	I	<i>TESS</i>
2458531.5679(13)	I	<i>TESS</i>	2459235.9768(1)	I	<i>TESS</i>	2458632.1010(12)	II	<i>TESS</i>
2458535.4569(12)	II	<i>TESS</i>	2459237.2664(6)	II	<i>TESS</i>	2458634.5172(1)	I	<i>TESS</i>
2458536.7471(5)	I	<i>TESS</i>	2459238.5666(1)	I	<i>TESS</i>	2458636.9324(4)	II	<i>TESS</i>
2458538.0450(4)	II	<i>TESS</i>	2459239.8576(9)	II	<i>TESS</i>	2458637.7373(7)	I	<i>TESS</i>
2458539.3370(6)	I	<i>TESS</i>	2459242.4475(6)	II	<i>TESS</i>	2458640.9578(2)	I	<i>TESS</i>
2458540.6353(2)	II	<i>TESS</i>	2459243.7460(1)	I	<i>TESS</i>	2458642.5679(2)	I	<i>TESS</i>
2459186.7712(20)	I	<i>V</i>	2459245.0356(10)	II	<i>TESS</i>	2458643.3735(6)	II	<i>TESS</i>
2459190.6528(2)	II	<i>I</i>	2459246.3357(1)	I	<i>TESS</i>	2458645.7883(1)	I	<i>TESS</i>
2459199.7204(15)	I	<i>B</i>	2459247.6254(8)	II	<i>TESS</i>	2458648.2045(2)	II	<i>TESS</i>
2459202.3102(1)	I	<i>TESS</i>	2459248.9255(1)	I	<i>TESS</i>	2458649.0087(8)	I	<i>TESS</i>

Table D.2. Table D.1 cont.

HJD	Type	Filter	HJD	Type	Filter	HJD	Type	Filter
V632 Sco			TT Vel					
2458650.6189(1)	I	TESS	2458544.5609(5)	II	TESS	2458586.7312(10)	II	TESS
2458651.4239(9)	II	TESS	2458545.6132(15)	I	TESS	2458587.7824(1)	I	TESS
2458652.2289(1)	I	TESS	2458546.6696(14)	II	TESS	2458588.8397(9)	II	TESS
2459024.9868(2)	II	V	2458547.7215(1)	I	TESS	2458589.8907(1)	I	TESS
2459032.2280(2)	I	B, V, I	2458548.7775(7)	II	TESS	2458590.9483(8)	II	TESS
2459066.0411(20)	I	B	2458549.8299(1)	I	TESS	2458591.9990(15)	I	TESS
2459362.3102(1)	I	TESS	2458550.8866(5)	II	TESS	2458593.0564(8)	II	TESS
2459363.9205(1)	I	TESS	2458551.9385(9)	I	TESS	2458594.1076(1)	I	TESS
2459364.7265(6)	II	TESS	2458552.9950(7)	II	TESS	2458595.1649(5)	II	TESS
2459365.5306(1)	I	TESS	2458554.0469(4)	I	TESS	2459281.4668(1)	I	TESS
2459366.3397(3)	II	TESS	2458555.1034(16)	II	TESS	2459282.5225(5)	II	TESS
2459367.1407(1)	I	TESS	2458557.2124(11)	II	TESS	2459283.5756(1)	I	TESS
2459367.9505(4)	II	TESS	2458558.2638(1)	I	TESS	2459284.6310(2)	II	TESS
2459368.7508(1)	I	TESS	2458559.3206(11)	II	TESS	2459285.6841(1)	I	TESS
2459369.5606(3)	II	TESS	2458560.3722(2)	I	TESS	2459286.7392(4)	II	TESS
2459370.3611(1)	I	TESS	2458561.4293(6)	II	TESS	2459287.7925(1)	I	TESS
2459371.1702(3)	II	TESS	2458562.4808(8)	I	TESS	2459288.8481(4)	II	TESS
2459371.9711(1)	I	TESS	2458563.5377(4)	II	TESS	2459289.9010(1)	I	TESS
2459372.7813(5)	II	TESS	2458564.5891(6)	I	TESS	2459290.9564(5)	II	TESS
2459373.5813(1)	I	TESS	2458565.6464(11)	II	TESS	2459292.0094(1)	I	TESS
2459374.3905(3)	II	TESS	2458566.6978(1)	I	TESS	2459294.1182(1)	I	TESS
2459376.0004(3)	II	TESS	2458567.7548(13)	II	TESS	2459295.1729(3)	II	TESS
2459376.8016(1)	I	TESS	2458570.9145(2)	I	TESS	2459296.2264(1)	I	TESS
2459378.4117(1)	I	TESS	2458571.9716(9)	II	TESS	2459297.2819(3)	II	TESS
2459379.2214(2)	II	TESS	2458573.0231(6)	I	TESS	2459298.3348(1)	I	TESS
2459380.0220(1)	I	TESS	2458574.0800(6)	II	TESS	2459299.3903(5)	II	TESS
2459380.8170(13)	II	TESS	2458575.1314(8)	I	TESS	2459300.4433(1)	I	TESS
2459381.6320(1)	I	TESS	2458576.1887(13)	II	TESS	2459301.4984(4)	II	TESS
2459382.4392(2)	II	TESS	2458577.2401(2)	I	TESS	2459302.5517(0)	I	TESS
2459383.2421(1)	I	TESS	2458578.2971(9)	II	TESS	2459303.6070(8)	II	TESS
2459384.8523(1)	I	TESS	2458579.3484(1)	I	TESS	2459304.6602(0)	I	TESS
2459385.6617(3)	II	TESS	2458580.4058(9)	II	TESS	2459305.7155(2)	II	TESS
2459386.4625(1)	I	TESS	2458581.4567(2)	I	TESS	2459329.9612(15)	I	B, V, I
2459387.2821(9)	II	TESS	2458584.6228(6)	II	TESS	2459331.0212(17)	II	B, V, I
			2458585.6737(10)	I	TESS	2459352.0925(17)	II	B, V, I

Appendix E: Complete pulsation models

This appendix contains three tables which list the detected frequencies in all available data sets for each system. In each table are listed: the increasing number (n), the value (f_n), the amplitude (A), the phase (Φ), the S/N , and the most possible combination of each detected frequency. Details about the frequency analysis can be found in Section 5.

Table E.1. Detected pulsation frequencies of the δ Scuti component of HM Pup in all data sets.

n	f_n (cycle d ⁻¹)	A (mmag)	Φ (°)	S/N	Combination	n	f_n (cycle d ⁻¹)	A (mmag)	Φ (°)	S/N	Combination
<i>B</i> -filter											
1	0.038(1)	5.9(1)	3(1)	33.4		12	34.741(3)	1.2(1)	237(5)	7.1	f_4+f_8
2	38.563(1)	5.5(1)	9(1)	27.6		13	32.982(3)	1.0(1)	143(6)	6.0	$f_6+f_7-f_5$
3	36.424(1)	3.8(1)	354(1)	23.3		14	35.641(3)	1.2(1)	311(6)	5.7	$f_3-f_{11}-f_8$
4	34.265(1)	2.7(1)	174(2)	17.0	$2f_3-f_2$	15	0.454(3)	1.6(1)	208(7)	5.5	$\sim f_{\text{orb}}$
5	0.098(1)	3.1(1)	91(2)	14.5	$\sim f_1$	16	31.879(4)	1.2(1)	47(7)	5.3	$f_3+f_{16}-f_{14}$
6	31.113(1)	2.5(1)	72(3)	12.4	$f_2-f_3-f_5$ or $\sim 5f_{\text{orb}}$	17	31.756(4)	0.9(1)	47(8)	4.6	$f_{16}-f_5$
7	1.997(2)	1.5(1)	206(3)	9.2	$\sim 5f_{\text{orb}}$	18	2.692(4)	0.8(1)	167(8)	4.0	$f_{14}-f_{13}$ or $\sim 7f_{\text{orb}}$
8	0.506(2)	1.6(1)	304(4)	9.5	$f_2-f_3-4f_{\text{orb}}$	19	4.542(4)	0.8(1)	97(8)	4.2	f_3-f_{16} or $\sim 12f_{\text{orb}}$
9	0.156(2)	1.7(1)	63(4)	8.0	$\sim f_5$	20	38.084(4)	0.8(1)	24(8)	4.0	f_2-f_8
10	34.355(2)	1.3(1)	37(5)	7.8	f_4+f_1	21	32.815(5)	0.8(1)	323(9)	4.2	$f_{13}-f_5$
11	0.205(2)	1.4(1)	126(5)	7.1	$\sim f_9$	22	37.154(5)	0.8(1)	13(9)	4.1	$2f_3-f_{14}$

Notes. The temporal zero-points for the computation of the phases for each pass-band were: JD2459180.0 (*B*, *V*, *I*) and JD2459193.0 (*TESS*).

Table E.2. Table E.1 cont.

n	f_n (cycle d ⁻¹)	A (mmag)	Φ (°)	S/N	Combination	n	f_n (cycle d ⁻¹)	A (mmag)	Φ (°)	S/N	Combination
<i>V</i> -filter						<i>TESS</i>					
1	0.421(1)	5.5(1)	328(1)	31.5	$\sim f_{\text{orb}}$	1	38.5622(1)	2.61(3)	7(1)	81.2	
2	38.563(1)	4.9(1)	14(1)	19.3		2	36.4196(2)	2.10(3)	14(1)	62.3	
3	36.417(1)	3.7(1)	49(2)	20.1		3	1.1584(2)	2.02(3)	156(1)	13.7	$3f_{\text{orb}}$
4	0.568(1)	3.7(1)	319(2)	15.7	$f_2-f_3-4f_{\text{orb}}$	4	0.0317(2)	1.92(3)	77(1)	8.9	
5	0.014(1)	2.8(1)	354(3)	17.5		5	34.2608(2)	1.41(3)	200(1)	42.2	$2f_2-f_1$
6	34.260(1)	2.0(1)	248(3)	8.8	$2f_3-f_2$	6	0.7733(3)	1.06(3)	286(2)	5.6	$2f_{\text{orb}}$
7	0.132(1)	1.8(1)	0(4)	10.9	f_4-f_1	7	31.1131(3)	0.96(3)	78(2)	37.7	$f_3+2f_5-f_1$
8	32.806(1)	1.4(1)	88(4)	5.3		8	35.6479(4)	0.91(3)	246(2)	27.0	f_2-f_6
9	31.110(1)	1.3(1)	92(5)	5.6	f_8-3f_4	9	34.3527(5)	0.70(3)	52(3)	21.0	f_5+2f_4
10	38.082(1)	1.2(1)	69(5)	4.5	$f_8+f_3-f_9$	10	33.7391(5)	0.63(3)	100(3)	21.0	$f_8-f_3-f_6$
11	2.186(1)	1.2(1)	199(6)	5.0	f_3-f_6	11	2.3154(5)	0.62(3)	194(3)	8.1	$2f_3$
12	34.353(2)	1.1(1)	51(7)	4.9	$f_6+f_7-f_5$	12	38.0850(7)	0.49(3)	16(4)	15.6	$2f_8+f_3-f_9$
13	33.693(1)	0.9(1)	49(6)	4.5	f_6-f_4	13	33.5800(8)	0.43(3)	140(4)	14.3	f_9-f_6
<i>I</i> filter						14	31.8850(8)	0.40(3)	9(5)	16.0	f_7+f_6
1	38.562(2)	2.7(1)	15(3)	12.6		15	3.0853(10)	0.34(3)	137(5)	6.4	$8f_{\text{orb}}$
2	36.416(2)	2.4(1)	86(3)	11.3		16	32.7497(11)	0.30(3)	202(6)	10.7	$2f_8-f_1$
3	2.171(3)	2.3(1)	7(4)	9.0	f_1-f_2	17	36.4216(11)	0.29(3)	186(6)	8.7	$\sim f_2$
4	1.786(3)	1.3(1)	122(4)	5.2	f_3+f_{orb}	18	35.5271(11)	0.29(3)	243(6)	8.3	f_9+f_3
5	0.376(4)	2.7(1)	246(5)	13.8	f_3-f_4 or $\sim f_{\text{orb}}$	19	30.9800(15)	0.22(3)	56(8)	8.5	$f_{13}+f_7-f_{10}$
6	31.111(5)	1.2(1)	129(7)	5.2	f_2-3f_4	20	31.5101(16)	0.21(3)	158(9)	8.2	$f_3+f_7-f_6$
7	34.287(6)	1.0(1)	88(8)	5.3	f_2-f_3	21	20.0784(16)	0.20(3)	119(9)	9.9	$3f_{19}-f_2$
8	0.871(6)	1.4(1)	283(8)	6.9	$2f_5$	22	32.8101(18)	0.19(3)	6(10)	6.5	$f_{16}+f_4$
9	1.059(7)	1.5(1)	350(9)	6.9	$3f_5$ or $\sim 3f_{\text{orb}}$	23	37.0601(22)	0.16(3)	310(12)	4.8	$2f_8-f_5$
10	37.324(7)	1.1(1)	66(9)	4.7	f_2+f_8	24	33.7526(22)	0.15(3)	142(12)	5.1	$\sim f_{10}$
11	34.753(7)	0.9(1)	299(10)	4.6	f_5+f_7	25	39.8768(22)	0.15(3)	137(12)	5.4	$f_3+f_2+f_{11}$
						26	31.1142(22)	0.15(3)	75(12)	5.9	$\sim f_7$

Notes. The temporal zeropoints for the computation of the phases for each pass-band were: JD2459180.0 (*B*, *V*, *I*) and JD2459193.0 (*TESS*).

Table E.3. The same as Table E.1, but for V632 Sco.

n	f_n (cycle d ⁻¹)	A (mmag)	Φ (°)	S/N	Combination	n	f_n (cycle d ⁻¹)	A (mmag)	Φ (°)	S/N	Combination
<i>B</i> -filter						<i>TESS</i>					
1	0.819(1)	3.6(2)	311(4)	8.9		1	23.7423(5)	1.79(4)	134(1)	23.5	
2	23.539(1)	3.0(2)	141(4)	7.8		2	2.4846(5)	1.72(4)	181(1)	13.2	$4f_{\text{orb}}$
3	3.548(1)	2.3(2)	280(6)	5.0		3	3.1069(6)	1.50(4)	273(2)	14.0	$5f_{\text{orb}}$
4	16.780(1)	2.2(2)	216(6)	6.1		4	0.1746(7)	1.22(4)	230(2)	5.6	
5	33.064(1)	2.3(2)	144(6)	7.2	$2f_4-f_{\text{orb}}$	5	16.6507(7)	1.14(4)	205(2)	17.3	
6	0.216(1)	2.2(2)	21(6)	5.5		6	4.3486(13)	0.63(4)	94(4)	7.8	$3f_2-f_3$
7	7.115(1)	1.9(2)	149(7)	5.0	$2f_3$	7	22.5038(14)	0.58(4)	164(4)	7.5	$f_1+f_3-f_6$
8	31.322(1)	1.5(2)	35(9)	4.6	f_5-f_{orb}	8	32.0532(15)	0.56(4)	70(4)	5.9	$f_7+2f_5-f_1$
9	53.324(2)	1.3(2)	60(10)	4.0	$2f_7+2f_8-f_2$	9	5.5894(19)	0.43(4)	283(6)	5.8	$9f_{\text{orb}}$
10	37.904(2)	1.3(2)	127(10)	4.2	$f_1+f_3+2f_4$	10	24.8052(21)	0.40(4)	335(6)	5.1	$f_7+f_2-f_4$
11	20.196(2)	1.3(2)	128(10)	5.0	$f_2+f_6-f_3$	11	26.0437(16)	0.54(4)	125(4)	7.9	$f_1+f_2-f_4$
<i>V</i> -filter						12	32.0127(21)	0.40(4)	326(6)	5.3	$\sim f_8$
1	23.432(13)	2.9(5)	81(9)	7.1							

Notes. The temporal zeropoints for the computation of the phases for each pass-band were: JD2459025.0 (*B*, *V*) and JD2459361.0 (*TESS*).

Table E.4. The same as Table E.1, but for TT Vel.

n	f_n (cycle d ⁻¹)	A (mmag)	Φ (°)	S/N	Combination	n	f_n (cycle d ⁻¹)	A (mmag)	Φ (°)	S/N	Combination
<i>B</i> -filter						4	11.6748(11)	4.8(5)	2(6)	4.8	$f_1+f_2+f_3$
1	3.0101(2)	17.6(4)	96(1)	25.8	$3f_{\text{orb}}$	5	6.0325(13)	4.0(5)	242(7)	4.7	$2f_1-3f_2$
2	3.2725(3)	10.8(4)	122(2)	15.1		6	12.3723(15)	3.5(5)	117(8)	4.5	f_2+f_4
3	1.9443(4)	8.3(4)	222(3)	12.5		7	0.9916(15)	3.7(5)	265(8)	4.2	$f_2+f_6-2f_5$
4	15.3267(7)	5.0(4)	171(5)	6.6	$2f_{\text{orb}}$	<i>TESS</i>					
5	8.9257(7)	5.2(4)	137(4)	5.3	$4f_1$	1	15.5020(4)	2.64(5)	36(1)	37.8	$3f_{\text{orb}}$
6	12.0160(8)	4.5(4)	212(5)	6.7		2	1.4248(4)	2.34(5)	214(1)	14.4	
7	16.5918(10)	3.6(4)	151(6)	4.4	$f_7-f_5-2f_1$	3	0.0288(8)	1.36(5)	198(2)	5.7	$2f_{\text{orb}}$
8	1.6196(8)	4.4(4)	300(5)	6.7		4	0.9478(10)	1.01(5)	58(3)	5.1	
<i>V</i> -filter						5	14.4616(11)	0.98(5)	150(3)	15.0	$f_1-f_4-2f_3$
1	0.9503(4)	13.5(5)	258(2)	29.0	$2f_2-2f_1-2f_3$	6	27.8644(12)	0.84(5)	338(3)	18.6	$3f_5-f_1$
2	3.5354(5)	10.9(5)	9(3)	19.5		7	27.7637(15)	0.68(5)	180(4)	14.8	f_6-2f_3
3	0.7564(7)	7.1(5)	177(4)	15.8		8	12.5193(16)	0.65(5)	175(4)	12.2	f_5-2f_4
4	3.6562(9)	5.7(5)	103(5)	10.3	$f_5-2f_1-2f_2$	9	29.6763(21)	0.50(5)	340(5)	10.2	f_7+2f_4
5	15.7337(14)	3.7(5)	71(7)	7.0		10	14.5538(20)	0.51(5)	14(5)	7.9	f_1-f_4
6	12.4535(13)	3.8(5)	26(7)	7.9	f_6-2f_1	11	27.0191(25)	0.41(5)	21(6)	9.7	f_5+f_8
7	27.7026(16)	3.3(5)	4(8)	6.1	f_5+3f_4	12	14.2795(22)	0.47(5)	208(6)	7.0	$f_4+f_7-f_5$
8	11.0764(17)	3.0(5)	253(9)	5.8	$f_5+2f_2-f_3$	13	15.3411(25)	0.42(5)	267(6)	5.9	f_6-f_8
9	23.0640(18)	2.9(5)	26(10)	4.3	$f_1+f_4+f_6$	14	14.2186(25)	0.41(5)	67(6)	6.1	$\sim f_{12}$
10	6.3650(16)	3.2(5)	185(9)	4.7		15	23.2011(33)	0.31(5)	349(8)	5.1	$f_{11}-f_4-2f_2$
<i>I</i> -filter						16	28.6083(35)	0.30(5)	11(9)	6.2	$2f_{12}$
1	4.0502(6)	8.7(5)	125(3)	8.4		17	23.4807(35)	0.30(5)	160(9)	5.1	$f_{15}+f_5-f_{14}$
2	0.6947(8)	6.6(5)	40(4)	7.8		18	25.9232(37)	0.28(5)	135(9)	5.9	$f_{11}+f_5-f_1$
3	3.1096(9)	5.7(5)	134(5)	5.4		19	15.4982(37)	0.28(5)	241(9)	5.1	$\sim f_1$

Notes. The temporal zeropoints for the computation of the phases for each pass-band were: JD2459325.0 (*B*, *V*, *I*) and JD2459281.0 (*TESS*).